

**Impacts of Convective Parameterization and Moisture Convective Trigger on
AGCM-Simulated Convectively Coupled Equatorial Waves**

Jia-Lin Lin¹, Myong-In Lee², Daehyun Kim³, and In-Sik Kang³

¹NOAA ESRL/CIRES Climate Diagnostics Center, Boulder, CO

²NASA GSFC Global Modeling and Assimilation Office, Greenbelt, MD

³School of Earth and Environmental Sciences, Seoul National University, Seoul, Korea

J. Climate, accepted with minor revisions
February 2007

Corresponding author address: Dr. Jia-Lin Lin
NOAA ESRL/CIRES Climate Diagnostics Center
325 Broadway, R/PSD1, Boulder, CO 80305-3328
Email: jjalin.lin@noaa.gov

Abstract

This study examines the impacts of convective parameterization and moisture convective trigger on convectively coupled equatorial waves simulated by the Seoul National University (SNU) atmospheric general circulation model (AGCM). Three different convection schemes are used including the relaxed Arakawa-Schubert (RAS) scheme, the Kuo scheme, and the moist convective adjustment (MCA) scheme, and a moisture convective trigger with variable strength is added to each scheme. We also conduct a “no convection” experiment with deep convection scheme totally turned off. Eight years of AMIP experiment for each model configuration are analyzed. Space-time spectral analysis is used to obtain the variance and phase speed of dominant convectively coupled equatorial waves, including the Madden-Julian Oscillation (MJO), Kelvin, equatorial Rossby (ER), mixed Rossby-gravity (MRG), and eastward inertio-gravity (EIG) and westward inertio-gravity (WIG) waves.

The results show that both convective parameterization and moisture convective trigger have significant impacts on AGCM-simulated convectively coupled equatorial waves. The MCA scheme generally produces larger variances of convectively coupled equatorial waves including MJO, more coherent eastward propagation of MJO, and more prominent MJO spectral peak than the KUO and SAS schemes. Increasing the strength of moisture trigger significantly enhances the variances and slows down the phase speeds of all wave modes except the MJO, and usually improves the eastward propagation of MJO for KUO and SAS schemes, but the effect for MCA scheme is small. The “no convection” experiment always produces one of the best signals of convectively coupled equatorial waves and the MJO.

1. Introduction

The tropical deep convection does not occur randomly, but is often organized by convectively coupled equatorial waves, such as the Madden-Julian Oscillation (Madden and Julian 1971), Kelvin, equatorial Rossby (ER), mixed Rossby-gravity (MRG), and eastward inertio-gravity (EIG) and westward inertio-gravity (WIG) waves (e.g. Takayabu 1994; Wheeler and Kiladis 1999, hereafter WK). These waves significantly affect a wide range of tropical weather such as the onset and breaks of the Indian and Australian summer monsoons (e.g. Yasunari 1979; Wheeler and McBride 2005), and the formation of tropical cyclones in almost all basins (e.g. Liebmann et al. 1994; Maloney and Hartmann 2000, 2001; Bessafi and Wheeler 2006). On a longer timescale, the convectively coupled equatorial waves also trigger or terminate some El Nino events (e.g. Kessler et al. 1995, Takayabu et al. 1999, Bergman et al. 2001; Roundy and Kiladis 2006). Therefore, these waves are important for both weather prediction and climate prediction.

Unfortunately, these convectively coupled equatorial waves are not well simulated in the general circulation models (GCMs) used for predictions and projections. For example, poor simulation of the MJO has been a well-known long-standing problem in GCMs, and the model MJOs are often too weak and propagate too fast (e.g. Hayashi and Sumi 1986; Hayashi and Golder 1986, 1988, Lau et al. 1988, Slingo et al. 1996; Waliser et al. 2003; Lin et al. 2006). The Atmospheric Model Intercomparison Project (AMIP) study by Slingo et al. (1996) found that no model has captured the dominance of the MJO in space-time spectral analysis found in observations, and nearly all have relatively more power at higher frequencies (<30 days) than in observations.

Recently, Lin et al. (2006) evaluates the tropical intraseasonal variability in 14 coupled GCMs participating in the Inter-governmental Panel on Climate Change (IPCC) Fourth Assessment Report (AR4). They evaluated not only the MJO, but also, for the first time in literature, other convectively coupled equatorial waves. The results show that current state-of-the-art GCMs still have significant problems and display a wide range of skill in simulating the tropical intraseasonal variability. The total intraseasonal (2-128 day) variance of precipitation is too weak in most of the models. About half of the models have signals of convectively coupled equatorial waves, with Kelvin and MRG-EIG waves especially prominent. However, the variances are generally too weak for all wave modes except the EIG wave, and the phase speeds are generally too fast, suggesting that these models may not have a large enough reduction in their “effective static stability” by diabatic heating. Most of the models produce overly weak MJO variance and poor MJO propagation. Moreover, the MJO variance in 13 of the 14 models does not come from a pronounced spectral peak, but usually comes from part of an over-reddened spectrum, which in turn is associated with too-strong persistence of equatorial precipitation. The two models that arguably do best at simulating the MJO are the only models having convective closures/triggers linked in some way to moisture convergence (i.e., the so-called Kuo-type closure/trigger).

Many observational studies have found clear signals of moisture preconditioning in MJO (e.g. Maloney and Hartmann 1998; Kemball-Cook and Weare 2001; Sperber 2003; Seo and Kim 2003; Myers and Waliser 2003; Kiladis et al. 2005; Tian et al. 2006). Consistently, many previous GCM studies have shown that adding a moisture trigger to the convection scheme can improve the simulations of MJO (e.g. Tokioka et al. 1988;

Itoh 1989; Wang and Schlesinger 1999; Lee et al. 2003; Zhang and Mu 2005). In a classic study, Wang and Schlesinger (1999) added a relative humidity criterion (RHc) to three different convection schemes: a modified version of the Arakawa-Schubert (1974) scheme, the Kuo (1974) scheme, and the moist convective adjustment (MCA) scheme of Manabe et al. (1965). They found that the simulated MJO is highly dependent on RHc. As RHc increases, the oscillations in the simulations become stronger for all three convection schemes. Using an aqua-planet version of a GCM, Lee et al. (2003) confirmed the results of Wang and Schlesinger (1999) and further studied the detailed convection structure simulated by three different convection schemes. They found that the MCA scheme tends to produce intense point-like convective storms, while the relaxed Arakawa-Schubert (RAS) scheme (Moorthi and Suarez 1992) tends to simulate low-intensity drizzling precipitation. The Kuo simulation lies in between. However, the impacts of moisture trigger on GCM simulated other convectively coupled equatorial waves (Kelvin, ER, MRG, EIG, and WIG) have not been studied by previous studies.

The purpose of this study is to extend the works of Wang and Schlesinger (1999) and Lee et al. (2003) to examine the effects of moisture trigger on AGCM-simulated convectively coupled equatorial waves. Three different convection schemes (RAS, Kuo, and MCA) are used, together with an experiment with convection scheme totally turned off (the “no-convection” experiment, i.e. only the large-scale condensation scheme is working). The questions we address are:

- (1) How do the simulated convectively coupled equatorial waves depend on the different convection schemes? Does the KUO scheme always produce good MJO signals as the IPCC models with KUO-type closure/trigger?

(2) What are the impacts of moisture trigger on the simulated convectively coupled equatorial waves?

(3) How is the “no-convection” experiment compared with the experiments with convection schemes?

The models and validation datasets used in this study are described in section 2. The diagnostic methods are described in section 3. Results are presented in section 4. A summary and discussion are given in section 5.

2. Models and validation datasets

The model used in this study is the Seoul National University atmospheric general circulation model (SNUGCM). The model is a global spectral model, with 20 vertical levels in a sigma coordinate. In this study, T42 ($\sim 2.8^\circ \times 2.8^\circ$) truncation is used for the model horizontal resolution. The standard deep convection scheme of the SNUGCM is a simplified version of the relaxed Arakawa-Schubert (SAS) scheme (Numaguti et al. 1995). The large-scale condensation scheme consists of a prognostic microphysics parameterization for total cloud liquid water (Le Treut and Li, 1991) with a diagnostic cloud fraction parameterization. Non-precipitating shallow convection scheme (Tiedtke 1983) is also implemented in the model for the mid-tropospheric moist convection. The boundary layer scheme is a non-local diffusion scheme based on Holtslag and Boville (1993), while the land surface model is from Bonan (1996). The radiation process is parameterized by the two-stream k distribution scheme implemented by Nakajima et al. (1995). Other details of the model physics are described in Lee et al. (2001, 2003).

To examine the effects of the convection parameterizations on the simulated convectively coupled equatorial waves, we tested the model with three different convection schemes with variable strength of moisture trigger functions. The basic closure assumption of the SAS scheme is same as that of Arakawa and Schubert (1974), where the intensity of the deep convection is parameterized by the sum of the cloud work functions (parcel buoyancies of the entraining convective plumes). Only positive cloud work functions can trigger moist convection. Following Tokioka et al. (1988), an additional trigger function was added to the standard SAS scheme, which constrains the entrainment rate of convective plumes (μ) as:

$$\mu_{\min} = \alpha / D, \quad (1)$$

where D is the depth of the planetary boundary layer and α is a non-negative constant. Only convective plumes of $\mu \geq \mu_{\min}$ are triggered in the cumulus ensemble. We increased the constant α for testing the strength of the moist convective trigger in the SAS scheme. The Kuo scheme assumes a fraction of b of total moisture convergence to the given atmospheric vertical column (Kuo 1974) as:

$$b = 1 - \frac{RH - RH_a}{RH_b - RH_a}, \quad (2)$$

that parameterized to moisten the atmosphere, whereas remaining $(1-b)$ rains out. In Eq. (2), RH denotes the column-mean relative humidity, and RH_a and RH_b are two constants that determine the strength of the moist convection trigger. As they increase, deep convection is getting harder to be triggered. The moist convective adjustment (MCA) of Manabe et al. (1965) simply trigger moist convection and restores the lapse rate to the moist adiabatic, if only the lapse rate of the two contiguous layers becomes moist convective unstable and saturated. Saturation condition is met when the grid-mean RH

exceeds the critical value (RH_c). In this study, various values of RH_c were tested to modify the convection trigger in the MCA scheme. Finally, the model was tested without deep convection scheme, where the simulated precipitation is solely generated by the large-scale condensation scheme.

Table 1 summarizes the various sensitivity experiments that analyzed in this study, and each run consists of 8 year AMIP-style simulations (1979-1986) driven by the same observed sea surface temperatures and sea-ice distributions.

The model simulations are validated using multiple observational datasets. To bracket the uncertainties associated with precipitation measurements/retrievals, especially the well-known difference between infrared (IR) based retrievals and microwave-based retrievals (e.g. Yuter and Houze 2000), we use two different precipitation datasets: (1) 8 years (1997-2004) of daily GOES Precipitation Index (GPI, Janowiak and Arkin 1991) precipitation with a horizontal resolution of 2.5 degree longitude by 2.5 latitude, which is retrieved based on IR measurements from multiple geostationary satellites; and (2) 8 years (1997-2004) of daily Global Precipitation Climatology Project (GPCP) One-Degree-Daily (1DD) Precipitation (Huffman et al. 2001) with a horizontal resolution of 1 degree longitude by 1 degree latitude. These are IR-based GPI retrievals scaled by the monthly means of microwave-based SSM/I retrievals.

3. Method

Through the space-time spectral analysis of outgoing longwave radiation (OLR), Takayabu (1994) and WK demonstrated that a significant portion of tropical cloudiness is organized in waves corresponding to the normal modes of the linear shallow water

system isolated by Matsuno (1966). In WK, these spectra represent the power remaining in the symmetric and antisymmetric components of OLR about the equator after dividing raw wavenumber-frequency power spectra by an estimate of the background power spectrum. Peaks standing above the background correspond to the Kelvin, $n=1$ equatorial Rossby (ER), mixed Rossby-gravity (MRG), $n=0$ eastward inertio-gravity (EIG), $n=1$ westward inertio-gravity (WIG) and $n=2$ WIG waves. It was found that the dispersion curves that best match the wavenumber-frequency characteristics of these waves have surprisingly shallow equivalent depths in the range of around 25 m, which is about an order of magnitude smaller than that expected for a free wave with a similar vertical wavelength twice the depth of the troposphere (e.g. Salby and Garcia 1987; Wheeler et al. 2000).

Using the methodology of WK, space-time spectra of daily tropical precipitation were obtained for the 8 years of model data used in this study and compared with those of eight years of observed precipitation estimates from the GPI and 1DD data sets. We will briefly outline this procedure here, and refer the reader to WK and Lin et al. (2006) for further details.

The model and validation precipitation data were first interpolated to a zonal resolution of 5 degrees longitude. We then decomposed the precipitation into its antisymmetric and symmetric components, averaged these from 15N to 15S, and computed spectra of the averaged values. To reduce noise the space-time spectra were calculated as in WK for successive overlapping segments of data and then averaged, here 128 days long with 78 days of overlap between each segment. Complex Fourier coefficients are first obtained in zonal planetary wavenumber space, which are then

subjected to a further complex FFT to obtain the wavenumber-frequency spectrum for the symmetric and antisymmetric components of precipitation about the equator.

An estimate of the "background" space-time spectrum is obtained for each data set by averaging the power of the symmetric and antisymmetric spectra and smoothing this by successive passes of a 1-2-1 filter in frequency and wavenumber (see WK). The raw spectra are then divided by this background to obtain an estimate of the signal standing above the background noise. Here we assume the signal is significant if it stands at 1.2 times (or 20% above) the background. It should be emphasized that, while this is only a rough estimate of the true "significance" of the signals, the intent is to simply identify those modes which might represent signals in rainfall standing above a simple red noise continuum that would presumably prevail if rainfall were not organized by disturbances on the large scale.

The definitions of Kelvin, ER, MRG, EIG and WIG modes are as in WK and Lin et al. (2006). Each mode was isolated by filtering in the wavenumber-frequency domain (see Fig. 6 of WK for the defined regions of filtering for each wave), and the corresponding time series were obtained by an inverse space-time Fourier transform.

As in Lin et al. (2006) the MJO is defined as significant rainfall variability in eastward wavenumber 1-6 and in the period range of 30-70 days. The variance of the MJO anomaly was also compared with the variance of its westward counterpart, i.e., the westward wavenumbers 1 through 6, 30-70 day anomaly, which was isolated using the same method as above.

4. Results

a Climatological precipitation in the equatorial belt

Previous observational studies indicate that the intraseasonal variance of convection is highly correlated with time-mean convective intensity (e.g. WK, Hendon et al. 1999). Therefore we first look at the eight-year time-mean precipitation along the equatorial belt, especially over the Indo-Pacific warm pool region, where most of the convectively coupled equatorial waves have the largest variance (WK). Figure 1 shows the annual mean precipitation versus longitude averaged between (a) 15N and 15S, and (b) 5N and 5S. To focus on the large-scale features, we smoothed the data zonally to retain only zonal wavenumbers 0 through 6. Figure 1 demonstrates two points. First, all experiments except KUO-1 simulate reasonably the basic feature of observed precipitation, with the primary maximum over the Indo-Pacific warm pool region, and a secondary local maximum over Central/South America. KUO-1, on the other hand, produces overly large precipitation over western Indian Ocean, eastern Pacific and Atlantic Ocean, which is similar to many IPCC AR4 models (Lin et al. 2006). Within the warm pool region, all experiments, except KUO-1 and SAS-0, reproduce the local minimum of precipitation over the maritime continent, but there is a positive bias over the western Pacific and a negative bias over the eastern Indian Ocean. Outside the warm pool region, all experiments produce quite realistic magnitude of precipitation over Central/South America. Comparing with the 15N-15S average (Figure 1a), the biases in 5N-5S average (Figure 1b) are smaller over western Pacific, but larger over eastern Indian Ocean.

Second, although in some cases (KUO-1 and SAS-0) adding/removing a moisture trigger causes significant change in climatological mean precipitation, in most of the

cases it has little effect on the mean precipitation (e.g. KUO-2 vs KUO-3; SAS-1, SAS-2 and SAS-3; all MCA experiments), and thus any difference in their intraseasonal variability is likely due to the moisture trigger instead of change in mean precipitation.

In short, the climatological precipitation over the Indo-Pacific warm pool is reasonably simulated by all experiments except KUO-1. Changing the moisture trigger has little effect on the climatological mean precipitation in most of the cases, suggesting that in those cases any change in the intraseasonal variability is likely due to change in moisture trigger instead of change in mean precipitation.

b Total intraseasonal (2-128 day) variance and raw space-time spectra

Figure 2 shows the total variance of the 2-128 day precipitation anomaly along the equator averaged between (a) 15N-15S, and (b) 5N-5S. There are two important things to note concerning Figure 2. First, despite the similar annual mean precipitation over the Indo-Pacific warm pool in all experiments except KUO-1 and SAS-0, the total intraseasonal variance displays a large scatter ranging from much smaller than observations to much larger than observations. There is a tendency for the models to have larger variance over the western Pacific than over the Indian Ocean, which is consistent with their tendency to have larger annual mean precipitation over the western Pacific (Figure 1). Among the three convection schemes, the MCA scheme tends to produce the largest variance, while the SAS scheme tends to produce the smallest variance and the KUO scheme lies in between. Interestingly, the NO CONV experiment also produces one of the largest variances, which is similar to the MCA experiments and the KUO-3 experiment with nearly saturated RH trigger.

Second, increasing the strength of moisture trigger significantly enhances the total intraseasonal variance for KUO scheme and SAS scheme. Note that KUO-1 produces one of the smallest 15N-15S variances over the whole Indo-Pacific warm pool (Figure 2a) although it simulates the largest 15N-15S annual mean precipitation over Indian Ocean (Figure 1a). It is also the case for SAS-0 which produces the largest 5N-5S mean precipitation over western Pacific (Figure 1b) but one of the smallest variances in that region (Figure 2b). However, increasing the strength of moisture trigger has little effect for the MCA scheme, which always produces the largest variances.

The symmetric space-time spectrum of the observational 1DD data is shown in Figure 3a where, as in WK, the plotted contours are the logarithm of the power. The spectrum is very similar in shape to those obtained by WK, even though WK used OLR instead of the blend of precipitation estimates comprising the 1DD dataset. As in WK, the spectrum is very red in time and space, with most power at the largest spatial scales and lowest frequencies. Despite this redness, distinct spectral peaks and gaps are evident even in this raw spectrum. One obvious feature is the dominance of eastward over westward power at low wavenumbers and frequencies, a signal corresponding to the MJO. Other peaks also correspond to known equatorial wave modes, and will be discussed further below.

The remainder of Figure 3 displays the corresponding spectra from the various model experiments, using identical contour intervals and shading as in Figs. 5a, and b (recall that these spectra are calculated for identical daily and 5 degree horizontal resolutions). Consistent with their total intraseasonal variances (Figure 2), the MCA scheme and NO CONV experiment produce the largest spectral powers in all frequencies and wavenumbers, while SAS scheme tends to simulate the smallest power, and the KUO

scheme lies in between. For both KUO scheme and SAS scheme, increasing the strength of moisture trigger significantly enhances the spectral power in all frequencies and wavenumbers. However, the effect is small for the MCA scheme. The characteristics of the raw antisymmetric spectra, in terms of total power and redness, are generally similar to Fig. 6 and so will not be shown here.

In summary, the MCA scheme and NO CONV experiment produce the largest total intraseasonal (2-128 day) variances of precipitation and the largest spectral powers in space-time spectrum. Increasing the strength of moisture trigger significantly enhances the total intraseasonal variance and spectral power for KUO and SAS schemes, but the effect for MCA scheme is small. The NO CONV experiment always produces one of the largest variances and spectral powers similar to the MCA experiments and the KUO-3 experiment with nearly saturated moisture trigger.

c Dominant intraseasonal modes

Figure 4 and Figure 5 show the results of dividing the symmetric and antisymmetric raw spectra by the estimates of their background spectra. This normalization procedure removes a large portion of the systematic biases within the various models and observed data sets in Figure 3, more clearly displaying the model disturbances with respect to their own climatological variance at each scale. Signals of the Kelvin, ER, and WIG waves are readily identified in the observational symmetric spectra (Figure 4a and b), along with the MRG and EIG waves in the antisymmetric spectra (Figure 5a and b). The MJO also appears as a prominent signal, especially in the symmetric spectra. Dispersion curves of the shallow water modes are also shown on all spectra, corresponding to equivalent depths of 12, 25, and 50 m. As in the OLR spectra of WK, all of the observed spectral

peaks corresponding to shallow water modes best match an equivalent depth of around 25 m in the observational rainfall data.

All experiments display signals of convectively coupled equatorial waves, with Kelvin and MRG-EIG waves especially prominent. For each experiment, all modes scale similarly to a certain equivalent depth, which is indicative of similar physical processes linking the convection and large-scale disturbances within each experiment. Increasing the strength of moisture trigger significantly slows down the phase speeds of Kelvin and MRG-EIG waves for both KUO and SAS schemes, but the effect is small for the MCA scheme. The NO CONV experiment simulates prominent wave signals which have the slowest phase speeds among all experiments.

When a model displays signals of a certain wave mode in Figure 4 and Figure 5, it means that the variance of that wave mode stands out above the background spectra (i.e., a high signal-to-noise ratio), but the absolute value of the variance of that wave mode may not be large. Therefore, it is of interest to look further at the absolute values of the variance of each wave mode. Figure 6 shows the variances of the (a) Kelvin, (b) ER, (c) MRG, (d) EIG, and (e) WIG modes along the equator averaged between 15N and 15S. There are three important conclusions that can be drawn from Figure 6. First, increasing the strength of moisture trigger significantly enhances the variance of all wave modes for both KUO and SAS schemes, but the effect is small and sometimes opposite for the MCA scheme. Second, the variance produced by the MCA scheme is always much larger than the observed variance. This is amazing since only one or two of the 14 IPCC AR4 models produce variances that are barely larger than observation. Third, the variance produced by

the NO CONV experiment is always among the largest, and is always much larger than the observed variance.

In summary, all experiments display signals of convectively coupled equatorial waves, with Kelvin and MRG-EIG waves especially prominent. For both KUO and SAS schemes, increasing the strength of moisture trigger significantly enhances the variances and slows down the phase speeds of all wave modes. However, the effect is small for the MCA scheme which always simulate prominent wave signals with variances much larger than observation. The NO CONV experiment also simulates prominent wave signals whose variances are among the largest, and phase speeds are the slowest.

d Variance of the MJO mode

Now we focus on the variance of the MJO mode, i.e., the daily variance in the MJO window of eastward wavenumbers 1-6 and periods of 30-70 days. Figure 7 shows the variance of the MJO anomaly along the equator averaged between (a) 15N and 15S, and (b) 5N and 5S. Figure 7 demonstrates four points. First, many experiments with moisture trigger produce quite large MJO variance that is close to or larger than the observed value over western Pacific. This is amazing considering the fact that only two of the 14 IPCC AR4 GCMs analyzed by Lin et al. (2006) simulate MJO variance that approaches the observed value. Second, although experiments with moisture trigger generally produce larger MJO variance than those without moisture trigger, increasing the strength of moisture trigger does not enhance monotonically the MJO variance, even for KUO and SAS schemes. For example, KUO-3 experiment produces smaller 15N-15S MJO variance than KUO-2 experiment over western Pacific, and so is SAS-4 versus SAS-3 (Figure 7a). This is in sharp contrast with the monotonic increase in the variances of other

wave modes for KUO and SAS schemes (Figure 6). For the MCA scheme, increasing the strength of moisture trigger even suppress the MJO variance over western Pacific, especially near the equator (Figure 7b), although the annual mean precipitation remains nearly the same (Figure 1b). Therefore, even though increasing the strength of moisture trigger always enhances the variances of other convectively coupled equatorial waves, one has to choose carefully a medium strength in order to get a strong MJO variance. Fourth, the NO CONV experiment always produces one of the largest variances, which is close or even larger than the observed value.

In addition to the variance of the eastward MJO, another important index for evaluating the MJO simulation is the ratio between the variance of the eastward MJO and that of its westward counterpart, i.e., the westward wavenumber 1 through 6, 30-70 day mode, which is important for the zonal propagation of tropical intraseasonal oscillation. Figure 8 shows the ratio between the eastward variance and the westward variance averaged over (a) an Indian Ocean box between 5N-5S and 70E-100E, and (b) a western Pacific box between 5N-5S and 140E-170E. In observations, the eastward MJO variance roughly triples the westward variance over both the Indian Ocean (Figure 8a) and the western Pacific (Figure 8b). Most of the experiments produce an overly small ratio. The MCA scheme often simulates a ratio larger than the other two schemes. Increasing the strength of moisture trigger generally increases the ratio for KUO and SAS schemes, but not for the MCA scheme. The NO CONV experiment always produces one of the largest ratios.

The competition between the eastward MJO variance and its westward counterpart largely determines the zonal propagation characteristics of tropical intraseasonal

oscillation. A useful method for evaluating the MJO simulation is to look at the propagation of 30-70 day filtered anomaly of the raw precipitation data, which includes all wavenumbers (zonal mean, eastward wavenumbers 1-6, westward wavenumbers 1-6, eastward wavenumbers 7 and up, westward wavenumbers 7 and up), to see if the MJO mode (the eastward wavenumbers 1-6 mode) dominates over other modes, as is the case in observations (e.g. Weickmann et al. 1985, 1997, Kiladis and Weickmann 1992, Lin and Mapes 2004). Because the tropical intraseasonal oscillation is dominated by zonally asymmetric, planetary-scale phenomena, the competition is mainly between the MJO and its westward counterpart - the westward wavenumbers 1-6 component. Figure 9 shows the lag-correlation of 30-70 day precipitation anomaly averaged between 5N and 5S with respect to itself at 0N85E. The observational data shows prominent eastward propagating signals of the MJO, with a phase speed of about 7 m/s. Consistent with the eastward/westward ratio in Figure 8a, most of the experiments can not reproduce the observed highly coherent eastward propagation. Nevertheless, increasing the strength of moisture trigger improves the eastward propagation for KUO and SAS schemes, although the phase speed is often too large especially for the SAS scheme. The MCA scheme generally produces more coherent eastward propagation than the other two schemes. The NO CONV experiment simulates the best eastward propagation although the phase speed is a little too slow. The results are similar when using a western Pacific reference point (not shown).

Next we apply more detailed scrutiny to the MJO precipitation variance by looking at the shape of the power spectrum. Figure 10a shows the raw spectra of the eastward wavenumber 1-6 component at 0N85E. Because it is difficult to see the shape of spectra

for several models with too small variance, we also plotted their normalized spectra (raw spectrum divided by its total variance) in Figure 10b. Both of the two observational datasets show prominent spectral peaks between 30 and 70 days periods, with the power of 1DD lower than that of GPI. Most of the experiments do not show a pronounced spectral peak in the MJO frequency band, but show too red of a spectrum, i.e., the variance of the MJO band does not stand above but is simply embedded within a red noise continuum. Increasing the strength of moisture trigger enhances the prominence of the spectral peak for the KUO scheme, but the effect is small for other schemes. The MCA scheme always produces to some degree a spectral peak with periods between 30-45 days. The NO CONV experiment simulates the most realistic spectral peak. Results for 0N155E (western Pacific) are similar (not shown).

The redness of the model spectra shown in Figure 10 brings to mind a “red noise” spectrum of a first-order linear Markov process (Gilman 1963; Jenkins and Watts 1968; Lin et al. 2006). For the first-order Markov process, the redness of the spectrum is determined by its lag-one auto-correlation ρ , which is hereafter referred to as the persistence of the time series. Therefore we plot in Figure 11 the auto-correlation function of precipitation at 0N85E. Both observational datasets have a ρ of about 0.7. The model experiments display a large scatter in the persistence of precipitation. The SAS scheme usually produces the largest persistence, while the MCA scheme usually produces the smallest persistence, and the KUO scheme lie in between. The NO CONV experiment simulates one of the smallest persistence. Increasing the strength of moisture trigger does not monotonically change the persistence. Results for 0N155E (western Pacific) are similar (not shown).

To summarize, the MCA scheme generally produces larger MJO variance, more coherent eastward propagation of MJO, and more prominent MJO spectral peak than the KUO and SAS schemes. Increasing the strength of moisture trigger does not monotonically enhance the MJO variance, but usually improves the eastward propagation of MJO for KUO and SAS schemes. The NO CONV experiment one of the most realistic MJO signals in terms of variance, eastward propagation and prominence of spectral peak.

5. Summary and discussion

This study examines the impacts of convective parameterization and moisture convective trigger on convectively coupled equatorial waves simulated by the SNU AGCM. Three different convection schemes are used including the RAS scheme, the Kuo scheme, and the MCA scheme, and a moisture convective trigger with variable strength is added to each scheme. We also conduct a “no convection” experiment with deep convection scheme totally turned off. Eight years of AMIP experiment for each model configuration are analyzed. Space-time spectral analysis is used to obtain the variance and phase speed of dominant convectively coupled equatorial waves, including the MJO, Kelvin, ER, MRG, EIG and WIG waves.

The results show that both convective parameterization and moisture convective trigger have significant impacts on AGCM-simulated convectively coupled equatorial waves. The MCA scheme generally produces larger variances of convectively coupled equatorial waves including MJO, more coherent eastward propagation of MJO, and more prominent MJO spectral peak than the KUO and SAS schemes. Increasing the strength of moisture trigger significantly enhances the variances and slows down the phase speeds of

all wave modes except the MJO, and usually improves the eastward propagation of MJO for KUO and SAS schemes, but the effect for MCA scheme is small. The “no convection” experiment always produces one of the best signals of convectively coupled equatorial waves and the MJO.

An interesting result of this study is that the “no convection” experiment always produces one of the best signals of convectively coupled equatorial waves and the MJO. In the early generations of GCMs, without deep convection scheme the model will blow up. But now with the improvement of dynamical cores, GCMs can work properly without deep convection scheme. Actually even when deep convection scheme is on, the large-scale condensation scheme is still in action and contributes to the total precipitation and heating. How does the large-scale condensation affect the experiments with deep convection scheme on? Figure 12 shows the ratio between time-mean large-scale precipitation and time-mean total precipitation averaged between (a) 15N-15S, and (b) 5N-5S. For the “no convection” experiment, as expected, all precipitation comes from large-scale precipitation and the ratio is always one. Strikingly, for the MCA scheme, about 90% of the precipitation comes from large-scale precipitation, and the ratio does not change much for different strengths of moisture trigger. In other words, although the MCA scheme is on, its contribution to the total heating is actually very small, and the experiments are basically quite similar to the “no convection” experiment. For Kuo and SAS schemes, when the moisture trigger becomes stronger and stronger, the ratio becomes larger and larger, making the experiment more and more similar to the “no convection” experiment. Therefore, *the better simulation of waves by the MCA scheme and the KUO and SAS schemes with strong moisture trigger is associated with the*

dominance of large-scale condensation in those experiments. The large-scale condensation scheme, by design, is very sensitive to environmental moisture. This further supports the importance of moisture control of deep convection for simulating the convectively coupled equatorial waves, although the effect may not be through the deep convection scheme, but is represented in the model by the large-scale condensation scheme.

How does the moisture control of deep convection enhance the convectively coupled equatorial waves? The moisture control can affect the waves by changing either the time-mean moisture field or the moisture anomaly associated with the waves. We plot in Figure 13 the time-mean total precipitable water (PW) along the equator. Except for the Kuo-1 experiment, there is no significant difference among different experiments for each scheme. For example, Kuo-2 and Kuo-3 experiments have nearly identical time-mean PW, but Kuo-3 has much stronger convectively coupled equatorial waves. All SAS experiments have similar mean PW, but increasing the strength of moisture trigger significantly improves the waves. Therefore, the effect of moisture trigger is not through changing the time-mean PW, but through changing the moisture anomaly associated with the waves.

Why, then, does the moisture anomaly affect the waves? It is widely accepted that wave-heating feedback plays a central role in amplifying and maintaining the convectively coupled equatorial waves. The column-integrated diabatic heating anomaly has six major components: the free troposphere moisture convergence, the boundary layer moisture convergence, the surface heat flux anomaly (latent plus sensible) due to wind variation, the local moisture tendency, the radiative heating, and the surface heat flux

anomaly due to SST variation. These six components have been emphasized by wave-CISK (e.g. Lau and Peng 1987), frictional wave-CISK (e.g. Wang and Rui 1990), WISHE (e.g. Emanuel 1987, Neelin et al. 1987), charge-discharge (e.g. Blade and Hartmann 1993), cloud-radiation interaction (e.g. Raymond 2001), and air-sea coupling (e.g. Flatau et al. 1997, Wang and Xie 1998; Waliser et al. 1999) theories, respectively. The moisture anomaly is involved in three of the above feedback mechanisms: the wave-CISK, frictional wave-CISK, and charge-discharge mechanisms. A stronger moisture trigger makes the moisture higher during deep convection which is associated with low-level convergence, and therefore increase the moisture convergence per unit mass convergence and enhance waves through the wave-CISK and frictional wave-CISK feedbacks. A stronger moisture trigger also prolongs the time for moisture to build up before deep convection can occur, and therefore increases the periods of the waves through the charge-discharge mechanism.

Acknowledgements

This study benefited much from discussions with Wanqiu Wang. J. L. Lin was supported by NOAA CPO/CVP Program, NOAA CPO/CDEP Program, and NASA MAP Program. In-Sik Kang and Daehyun Kim have been supported by Climate Environment System Research Center, sponsored by KOSEF, and the BK21 program.

REFERENCES

- Arakawa, A., and W. H. Schubert, 1974: Interaction of a cumulus cloud ensemble with the large scale environment. Part I. *J. Atmos. Sci.*, **31**, 674–701.
- Bergman, J. W., H. H. Hendon, K. M. Weickmann, 2001: Intraseasonal Air-Sea Interactions at the Onset of El Nino. *J. Climate*, **14**, 1702-1719.
- Bessafi, M. and M.C. Wheeler, 2005: Modulation of south Indian Ocean tropical cyclones by the Madden-Julian oscillation and convectively-coupled equatorial waves. *Mon. Wea. Rev.*, in press.
- Blade, I., and D. L. Hartmann, 1993: Tropical intraseasonal oscillations in a simple nonlinear model. *J. Atmos. Sci.*, **50**, 2922-2939.
- Bonan, G. B., A land surface model (LSM version 1.0) for ecological, hydrological, and atmospheric studies: Technical description and user's guide. NCAR *Tech. Note NCAR/TN-417+STR*, Natl. Cent. For Atmos. Res., 150pp., Boulder, Colorado.
- Bougeault, P., 1985: A Simple Parameterization of the Large-Scale Effects of Cumulus Convection. *Monthly Weather Review*, **113**, 2108–2121.
- Brown, R. G., and C. Zhang, 1997: Variability of midtropospheric humidity and its effect on cloud-top height distribution during TOGA COARE. *J. Atmos. Sci.*, **54**, 2760-2774.
- Del Genio, A. D., and M.-S. Yao, 1993: Efficient cumulus parameterization for long-term climate studies: The GISS scheme. *The Representation of Cumulus Convection in Numerical Models, Meteor. Monogr.*, No. 46, Amer. Meteor. Soc., 181–184.
- Dickinson, M., and Molinari J., 2002: Mixed Rossby–gravity waves and western Pacific tropical cyclogenesis. Part I: Synoptic evolution. *J. Atmos. Sci.*, **59**, 2183–2196.

- Duchan, C.E., 1979: Lanczos filtering in one and two dimensions. *J. Appl. Meteor.*, **18**, 1016-1022.
- Emanuel, K. A., J. D. Neelin, and C. S. Bretherton, 1994: On large-scale circulations in convecting atmospheres. *Quart. J. Roy. Meteor. Soc.*, **120**, 1111–1143.
- Flatau, M., P.J. Flatau, P. Phoebus, and P.P. Niiler, 1997: The feedback between equatorial convection and local radiative and evaporative processes: The implications for intraseasonal oscillations. *J. Atmos. Sci.*, **54**, 2373-2386.
- Haertel, P. T., and G. N. Kiladis, 2004: On the dynamics of two-day equatorial disturbances. *J. Atmos. Sci.*, submitted.
- Hayashi, Y., and A. Sumi, 1986: The 30-40 day oscillation simulated in an "aqua planet" model. *J. Meteor. Soc. Japan.*, **64**, 451-466.
- Hayashi, Y., and D. G. Golder, 1986: Tropical intraseasonal oscillations appearing in a GFDL general circulation model and FGGE data. Part I: Phase propagation. *J. Atmos. Sci.*, **43**, 3058-3067.
- Hayashi, Y., and D. G. Golder, 1988: Tropical intraseasonal oscillations appearing in a GFDL general circulation model and FGGE data. Part II: Structure. *J. Atmos. Sci.*, **45**, 3017-3033.
- Hendon, H.H., C. Zhang, and J.D. Glick, 1999: Interannual variation of the MJO during austral summer. *J. Climate*, **12**, 2538-2550.
- Holtlag, A. A. M., and B. A. Boville, 1993: Local versus nonlocal boundary layer diffusion in a global climate model. *J. Clim.*, **6**, 1825-1642.

- Huffman, G.J., R.F. Adler, M.M. Morrissey, S. Curtis, R. Joyce, B. McGavock, and J. Susskind, 2001: Global precipitation at one-degree daily resolution from multi-satellite observations. *J. Hydrometeor.*, **2**, 36-50.
- Janowiak, J. E., and P. A. Arkin, 1991: Rainfall variations in the Tropics during 1986-1989, as estimated from observations of cloud-top temperatures. *J. Geophys. Res.*, **96** (Suppl.), 3359-3373.
- Kessler, W. S., and M. J. McPhaden, and K. M. Weickmann, 1995: Forcing of intraseasonal Kelvin waves in the equatorial Pacific. *J. Geophys. Res.*, **100**, 10613-10631.
- Kemball-Cook S.R., and B.C. Weare, 2001: The onset of convection in the Madden-Julian oscillation. *J. Climate*, **14**, 780–793.
- Kiladis, G. N., K. H. Straub, and P. T. Haertel, 2005: Zonal and vertical structure of the Madden-Julian Oscillation. *J. Atmos. Sci.*, in press.
- Knutson, T. R., and K. M. Weickmann, 1987: 30–60 Day Atmospheric Oscillations: Composite Life Cycles of Convection and Circulation Anomalies. *Monthly Weather Review*, **115**, 1407–1436.
- Knutson, T. R., Klaus M. Weickmann and John E. Kutzbach. 1986: Global-Scale Intraseasonal Oscillations of Outgoing Longwave Radiation and 250 mb Zonal Wind during Northern Hemisphere Summer. *Monthly Weather Review*, **114**, 605–623.
- Kuo, Y. H., 1974: Further studies of the parameterization of the influence of cumulus convection of large-scale flow. *J. Atmos. Sci.*, **31**, 1232–1240.

- Lau, K. M., and P. H. Chan, 1985: Aspects of the 40-50-day oscillation during the northern winter as inferred from outgoing longwave radiation. *Mon. Wea. Rev.*, **113**, 1889-1909.
- Lau, K. M., and L. Peng, 1987: Origin of low-frequency (intraseasonal) oscillations in the tropical atmosphere. *J. Atmos. Sci.*, **44**, 950-972.
- Lau, N. C., I. M. Held, and J. D. Neelin, 1988: The Madden-Julian oscillations in an idealized general circulation model. *J. Atmos. Sci.*, **45**, 3810-3831.
- Lee, M.-I., I.-S. Kang, J.-K. Kim, and B. E. Mapes, 2001: Influence of cloud-radiation interaction on simulating tropical intraseasonal oscillation with an atmospheric general circulation model, *J. Geophys. Res.*, **106**, 14219-14233.
- Lee, M.-I., I.-S. Kang, and B.E. Mapes, 2003: Impacts of cumulus convection parameterization on aqua-planet AGCM simulations of tropical intraseasonal variability. *J. Meteor. Soc. Japan*, **81**, 963-992.
- Le Treut, H., and Z. -X. Li, 1991: Sensitivity of an atmospheric general circulation model to prescribed SST changes: feedback effects associated with the simulation of cloud optical properties. *Clim. Dyn.*, **5**, 175-187.
- Liebmann, B., H. H. Hendon, and J. D. Glick, 1994: The relationship between the tropical cyclones of the western Pacific and Indian Oceans and the Madden-Julian oscillation. *J. Meteor. Soc. Japan*, **72**, 401-411.
- Lin, J. L., 2006: The double-ITCZ problem in IPCC AR4 coupled GCMs: Ocean-atmosphere feedback analysis. *J. Climate*, accepted with minor revisions. Pdf file available at <http://www.cdc.noaa.gov/people/jialin.lin/>

- Lin, J. L., and B. E. Mapes, 2004: Radiation budget of the tropical intraseasonal oscillation. *J. Atmos. Sci.*, **61**, 2050-2062.
- Lin, J. L., B. E. Mapes, M. H. Zhang and M. Newman, 2004: Stratiform precipitation, vertical heating profiles, and the Madden-Julian Oscillation. *J. Atmos. Sci.*, **61**, 296-309.
- Lin, J. L., M. H. Zhang, and B. E. Mapes, 2005: Zonal momentum budget of the Madden-Julian Oscillation: The sources and strength of equivalent linear damping. *J. Atmos. Sci.*, **62**, 2172-2188.
- Lin, J. L., G.N. Kiladis, B.E. Mapes, K.M. Weickmann, K.R. Sperber, W.Y. Lin, M. Wheeler, S.D. Schubert, A. Del Genio, L.J. Donner, S. Emori, J.-F. Guérémy, F. Hourdin, P.J. Rasch, E. Roeckner, and J.F. Scinocca, 2006: Tropical intraseasonal variability in 14 IPCC AR4 climate models. Part I: Convective signals. *J. Climate*, **19**, 2665-2690.
- Madden, R. A., and P. R. Julian, 1971: Detection of a 40-50 day oscillation in the zonal wind in the tropical Pacific. *J. Atmos. Sci.*, **28**, 702-708.
- Maloney, E. D., and D. L. Hartmann, 1998: Frictional Moisture Convergence in a Composite Lifecycle of the Madden-Julian Oscillation. *Journal of Climate*, **11**, 2387-2403.
- Maloney, E. D., and D. L. Hartmann, 2000: Modulation of eastern North Pacific hurricanes by the Madden-Julian oscillation. *J. Climate.*, **13**, 1451–1460.
- Maloney, E. D., Hartmann, D. L. 2001: The Madden-Julian Oscillation, Barotropic Dynamics, and North Pacific Tropical Cyclone Formation. Part I: Observations. *J. Atmos. Sci.*, **58**, 2545-2558.

- Manabe, S. J., J. S. Smagorinsky, and R. F. Stricker, 1965: Simulated climatology of a general circulation model with a hydrological cycle. *Mon. Wea. Rev.*, **93**, 769–798.
- Mapes, B. E., and R. A. Houze, 1995: Diabatic divergence profiles in western Pacific mesoscale convective systems. *J. Atmos. Sci.*, **52**, 1807–1828.
- Mapes, B. E., and J. L. Lin, 2005: Doppler radar observations of mesoscale wind divergence in regions of tropical convection. *Mon. Wea. Rev.*, in press.
- Moorthi, S., and Suarez M. J., 1992: Relaxed Arakawa–Schubert: A parameterization of moist convection for general circulation models. *Mon. Wea. Rev.*, **120**, 978–1002.
- Murakami, M., 1979: Large-scale aspects of deep convective activity over the GATE area. *Mon. Wea. Rev.*, **107**, 994–1013.
- Myers D.S., and D.E. Waliser, 2003: Three-dimensional water vapor and cloud variations associated with the Madden–Julian oscillation during Northern Hemisphere winter. *J. Climate*, **16**, 929–950.
- Nakajima, T., M. Tsukamoto, Y. Tsushima, and A. Numaguti, 1995: Modelling of the radiative processes in an AGCM, in *Climate System Dynamics and Modelling*, vol. I-3, edited by T. Matsuno, pp. 104–123, Univ. of Tokyo, Tokyo.
- Neelin, J. D., and I. M. Held. 1987: Modeling Tropical Convergence Based on the Moist Static Energy Budget. *Monthly Weather Review*, **115**, 3–12.
- Numaguti, A., M. Takahashi, T. Nakajima, and A. Sumi, 1995: Development of an atmospheric general circulation model, in *Climate System Dynamics and Modelling*, vol. I-3, edited by T. Matsuno, pp. 1–27, Univ. of Tokyo, Tokyo.
- Oort, A. H., and J. J. Yienger, 1996: Observed long-term variability in the Hadley circulation and its connection to ENSO. *J. Climate*, **9**, 2751–2767.

- Raymond, D. J., 2001: A New Model of the Madden-Julian Oscillation. *J. Atmos. Sci.*, 58, 2807-2819.
- Schubert, S., R. Dole, H.v.d. Dool, M. Suarez, and D. Waliser, 2002: Proceedings from a workshop on "Prospects for improved forecasts of weather and short-term climate variability on subseasonal (2 week to 2 month) time scales", 16-18 April 2002, Mitchellville, MD, NASA/TM 2002-104606, vol. 23, pp. 171.
- Seo K.-H., and K.-Y. Kim, 2003: Propagation and initiation mechanisms of the Madden-Julian oscillation. *J. Geophys. Res.*, 108, 4384, doi:10.1029/2002JD002876.
- Slingo, J. M., and Coauthors, 1996: Intraseasonal oscillations in 15 atmospheric general circulation models: Results from an AMIP diagnostic subproject. *Climate Dyn.*, 12, 325-357.
- Straub, K. H., and George N. Kiladis. 2003: Interactions between the Boreal Summer Intraseasonal Oscillation and Higher-Frequency Tropical Wave Activity. *Monthly Weather Review*, 131, 945-960.
- Takayabu, Y. N., 1994: Large-scale cloud disturbances associated with equatorial waves. Part I: Spectral features of the cloud disturbances. *J. Meteor. Soc. Japan*, 72, 433-448.
- Takayabu, Y. N., T. Iguchi, M. Kachi, A. Shibata, and H. Kanzawa, 1999: Abrupt termination of the 1997-98 El Nino in response to a Madden-Julian oscillation. *Nature*, 402, 279-282.
- Tian, B., D. E. Waliser, E. J. Fetzer, B. H. Lambrigtsen, Y. Yung, and B. Wang, 2006: Vertical moist thermodynamic structure and spatial-temporal evolution of the MJO in AIRS observations. *J. Atmos. Sci.*, 63, 2462-2485.

- Tiedtke, M., 1983: The sensitivity of the time-mean large-scale flow to cumulus convection in the ECMWF model. *Workshop on Convection in Large-Scale Numerical Models*. ECMWF, 28 Nov-1 Dec 1983, pp297-316.
- Tiedtke, M., 1989: A comprehensive mass flux scheme for cumulus parameterization in large-scale models. *Mon. Wea. Rev.*, **117**, 1779-1800.
- Tokioka, T., K. Yamazaki, A. Kitoh, and T. Ose, 1988: The equatorial 30-60-day oscillation and the Arakawa-Schubert penetrative cumulus parameterization. *J. Meteor. Soc. Japan*, **66**, 883-901.
- Waliser, D.E., K.M. Lau, and J.H. Kim, 1999: The influence of coupled sea surface temperatures on the Madden-Julian oscillation: A model perturbation experiment. *J. Atmos. Sci.*, **56**, 333-358.
- Waliser, D., S. Schubert, A. Kumar, K. Weickmann, and R. Dole, 2003b: Proceedings from a workshop on "Modeling, Simulation and Forecasting of Subseasonal Variability", NASA/CP 2003-104606, vol. 25, pp. 62.
- Wang, B., and H. Rui, 1990: Dynamics of the coupled moist Kelvin-Rossby wave on an equatorial B-plane. *J. Atmos. Sci.*, **47**, 398-413.
- Wang, B., and X. Xie, 1998: Coupled modes of the warm pool climate system. Part I: The role of air-sea interaction in maintaining Madden-Julian oscillations. *J. Climate*, **8**, 2116-2135.
- Wang, W., and M.E. Schlesinger, 1999: The dependence on convective parameterization of the tropical intraseasonal oscillation simulated by the UIUC 11-layer atmospheric GCM. *J. Climate*, **12**, 1423-1457.

- Weickmann, K. M., G. R. Lussky, and J. E. Kutzbach, 1985: Intraseasonal (30-60 day) fluctuations of outgoing longwave radiation and 250 mb streamfunction during northern winter. *Mon. Wea. Rev.*, **113**, 941-961.
- Wheeler, M., and G.N. Kiladis, 1999: Convectively Coupled Equatorial Waves: Analysis of Clouds and Temperature in the Wavenumber-Frequency Domain. *J. Atmos. Sci.*, **56**, 374-399.
- Wheeler, M., G.N. Kiladis, and P.J. Webster, 2000: Large-scale dynamical fields associated with convectively coupled equatorial waves. *J. Atmos. Sci.*, **57**, 613-640.
- Wheeler, M.C., and J.L. McBride, 2005: Australian-Indonesian monsoon. *Intraseasonal Variability in the Atmosphere-Ocean Climate System*. W.K.M. Lau and D.E. Waliser (Eds.), Praxis Publishing, pp 125-173.
- Yasunari, T., 1979: Cloudiness fluctuations associated with the northern hemisphere summer monsoon. *J. Meteor. Soc. Japan*, **57**, 227-242.
- Yuter, S. E., and R. A. Houze Jr., 2000: The 1997 Pan American Climate Studies Tropical Eastern Pacific Process Study. Part I: ITCZ Region. *Bulletin of the American Meteorological Society*, **81**, 451-481.
- Zhang, G. J., and M. Mu, 2005: Simulation of the Madden-Julian Oscillation in the NCAR CCM3 using a revised Zhang-McFarlane convection parameterization scheme. *J. Climate*, **18**, 4046-4064.

FIGURE CAPTIONS

Figure 1. Annual mean precipitation along the equatorial belt averaged between (a) 15N and 15S, and (b) 5N and 5S for two observational datasets and 14 models. The data are smoothed zonally to keep only wavenumber 0-6. The locations of continents within the equatorial belt are indicated by black bars under the abscissa.

Figure 2. Variance of the 2-128 day precipitation anomaly along the equator averaged between (a) 15N-15S, and (b) 5N-5S.

Figure 3. Space-time spectrum of 15N-15S symmetric component of precipitation. Frequency spectral width is 1/128 cpd.

Figure 4. Space-time spectrum of 15N-15S symmetric component of precipitation divided by the background spectrum. Superimposed are the dispersion curves of the odd meridional mode-numbered equatorial waves for the five equivalent depths of 12, 25, and 50m. Frequency spectral width is 1/128 cpd.

Figure 5. As in Figure 4 except for 15N-15S antisymmetric component of precipitation.

Figure 6. Variances of (a) Kelvin, (b) ER, (c) MRG, (d) EIG, and (e) WIG modes along the equator averaged between 15N and 15S.

Figure 7. Variance of the MJO mode along the equator averaged between (a) 15N and 15S, and (b) 5N and 5S.

Figure 8. Ratio between the MJO variance and the variance of its westward counterpart (westward wavenumber 1-6, 30-70 day mode). The variances are averaged over (a) an Indian Ocean box between 5N-5S and 70E-100E, and (b) a western Pacific box between 5N-5S and 140E-170E.

Figure 9. Lag-correlation of the 30-70 day precipitation anomaly averaged along the equator between 5N and 5S with respect to itself at 0N85E. The three thick lines correspond to phase speed of 3, 7, and 15 m/s, respectively.

Figure 10. Spectrum of the eastward wavenumber 1-6 component of equatorial precipitation (5N-5S) at 0N155E for two observational datasets and 14 models. (a) raw spectrum; (b) normalized spectrum. Frequency spectral width 1/100 cpd.

Figure 11. Auto-correlation of precipitation at 0N155E.

Figure 12. The ratio between time-mean large-scale precipitation and time-mean total precipitation averaged between (a) 15N-15S, and (b) 5N-5S.

Figure 13. Annual mean total precipitable water along the equator averaged between 5N and 5S.

Table 1 Description of the sensitivity experiments to the convection scheme and its moist trigger function.

Deep convection scheme	Experiment	Moisture trigger
KUO	KUO-1	RHa=0, RHb=10
	KUO-2	RHa=80, RHb=90
	KUO-3	RHa=90, RHb=95
Simplified Arakawa-Schubert (SAS)	SAS-0	$\alpha=0$
	SAS-1	$\alpha=0.05$
	SAS-2	$\alpha=0.1$
	SAS-3	$\alpha=0.2$
Moist convective adjustment (MCA)	MCA-1	RHc=60
	MCA-2	RHc=80
	MCA-3	RHc=99
No deep convection	NO CONV	

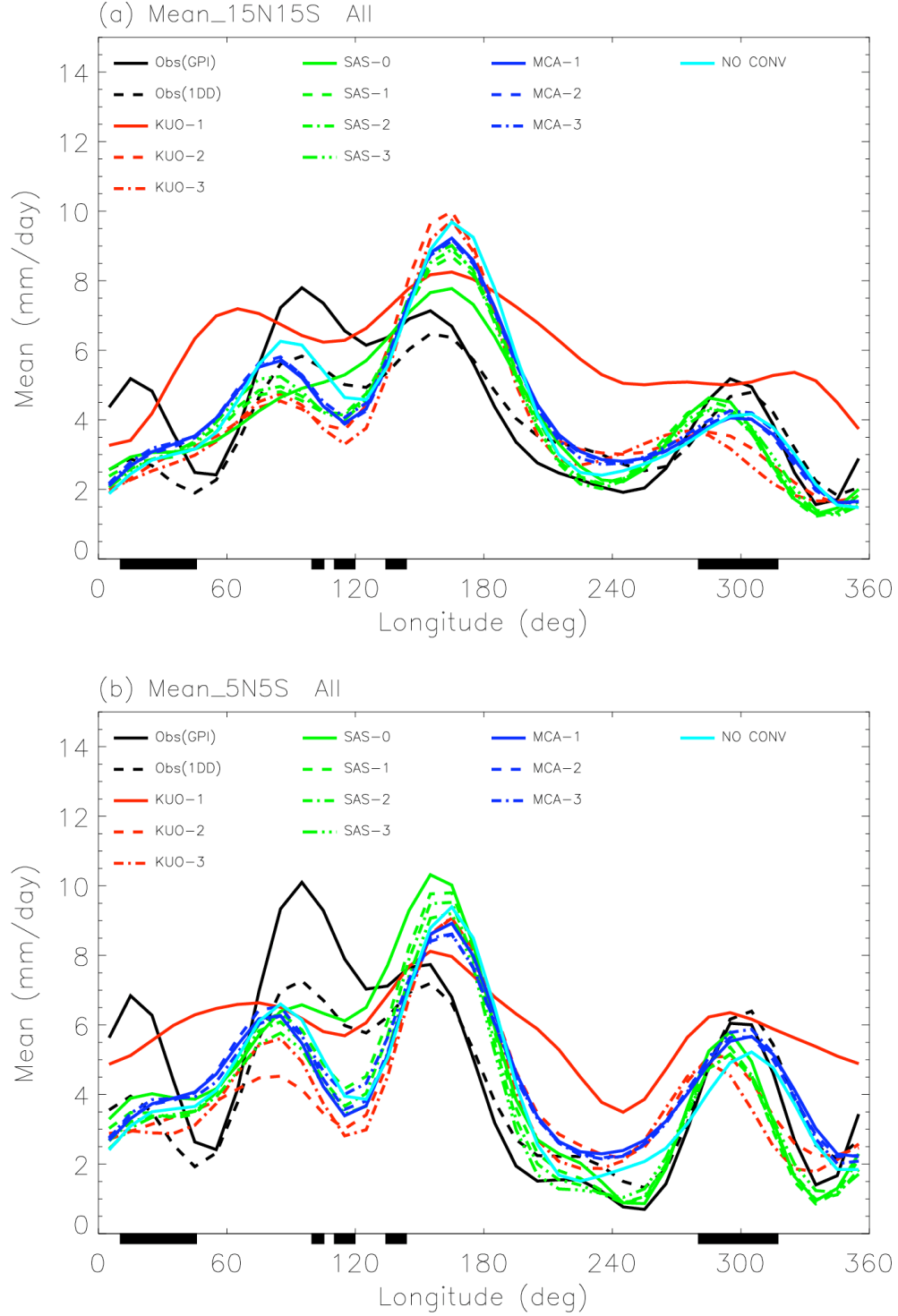


Figure 1. Annual mean precipitation along the equatorial belt averaged between (a) 15N and 15S, and (b) 5N and 5S for two observational datasets and 14 models. The data are smoothed zonally to keep only wavenumber 0-6. The locations of continents within the equatorial belt are indicated by black bars under the abscissa.

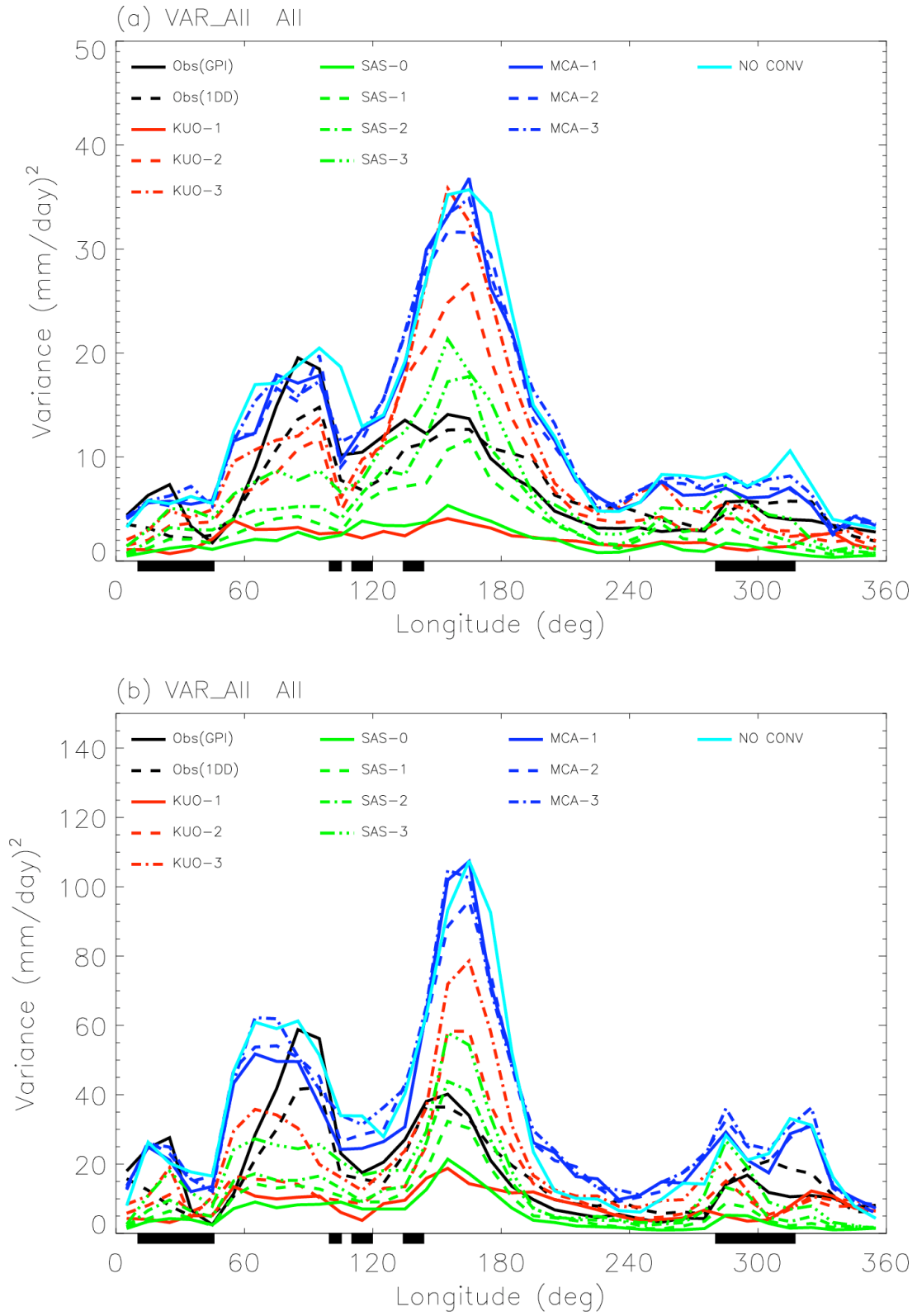


Figure 2. Variance of the 2-128 day precipitation anomaly along the equator averaged between (a) 15N-15S, and (b) 5N-5S.

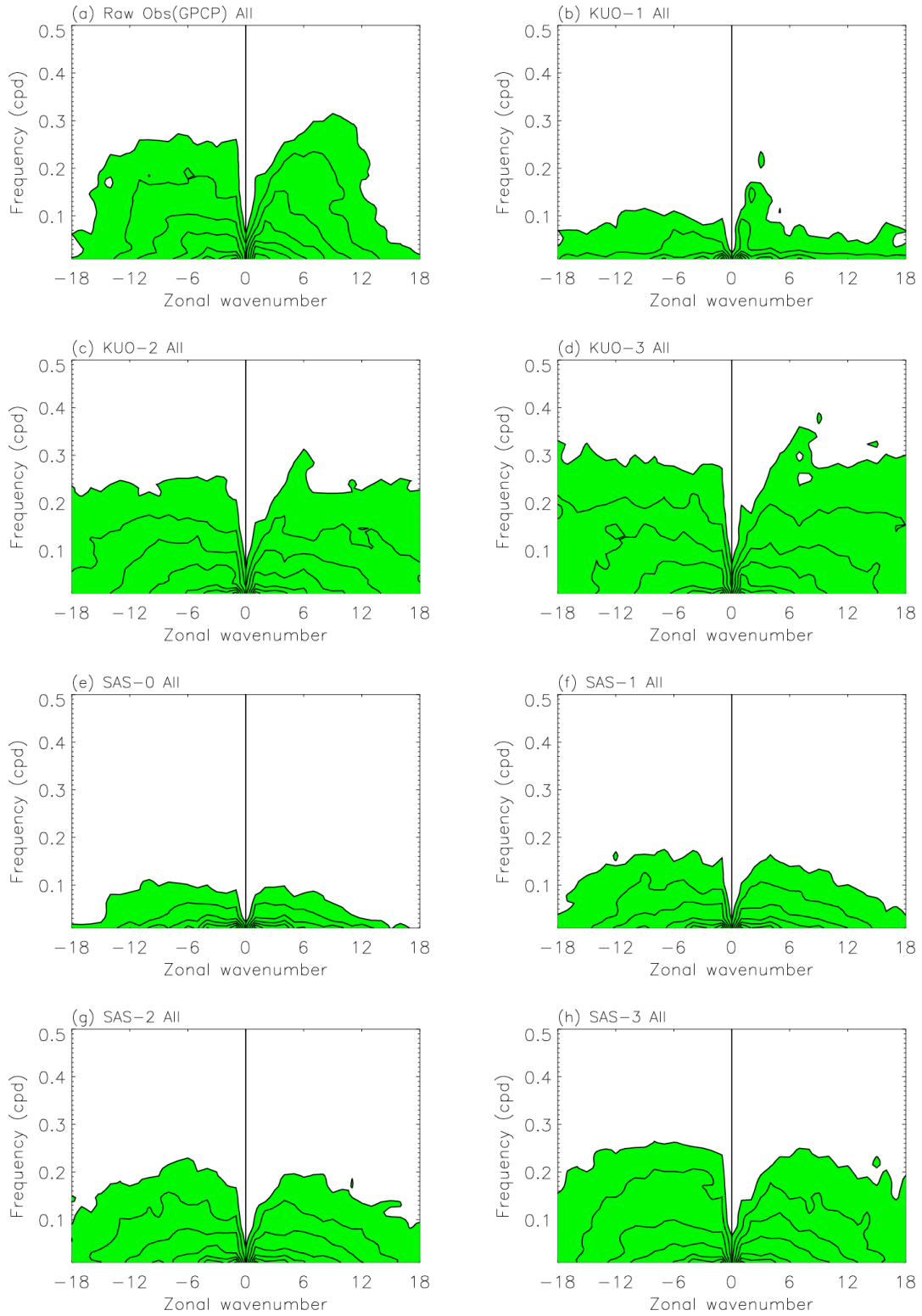


Figure 3. Space-time spectrum of 15N-15S symmetric component of precipitation. Frequency spectral width is 1/128 cpd.

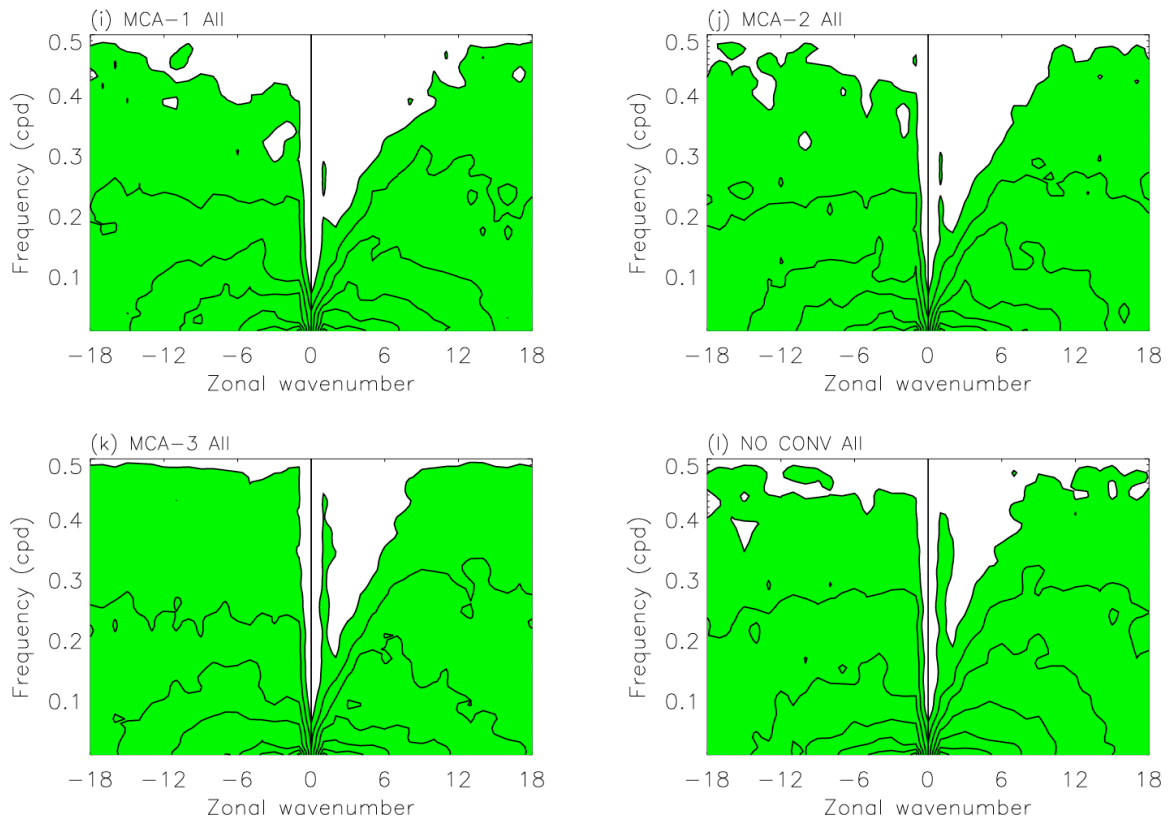


Figure 3. Continued.

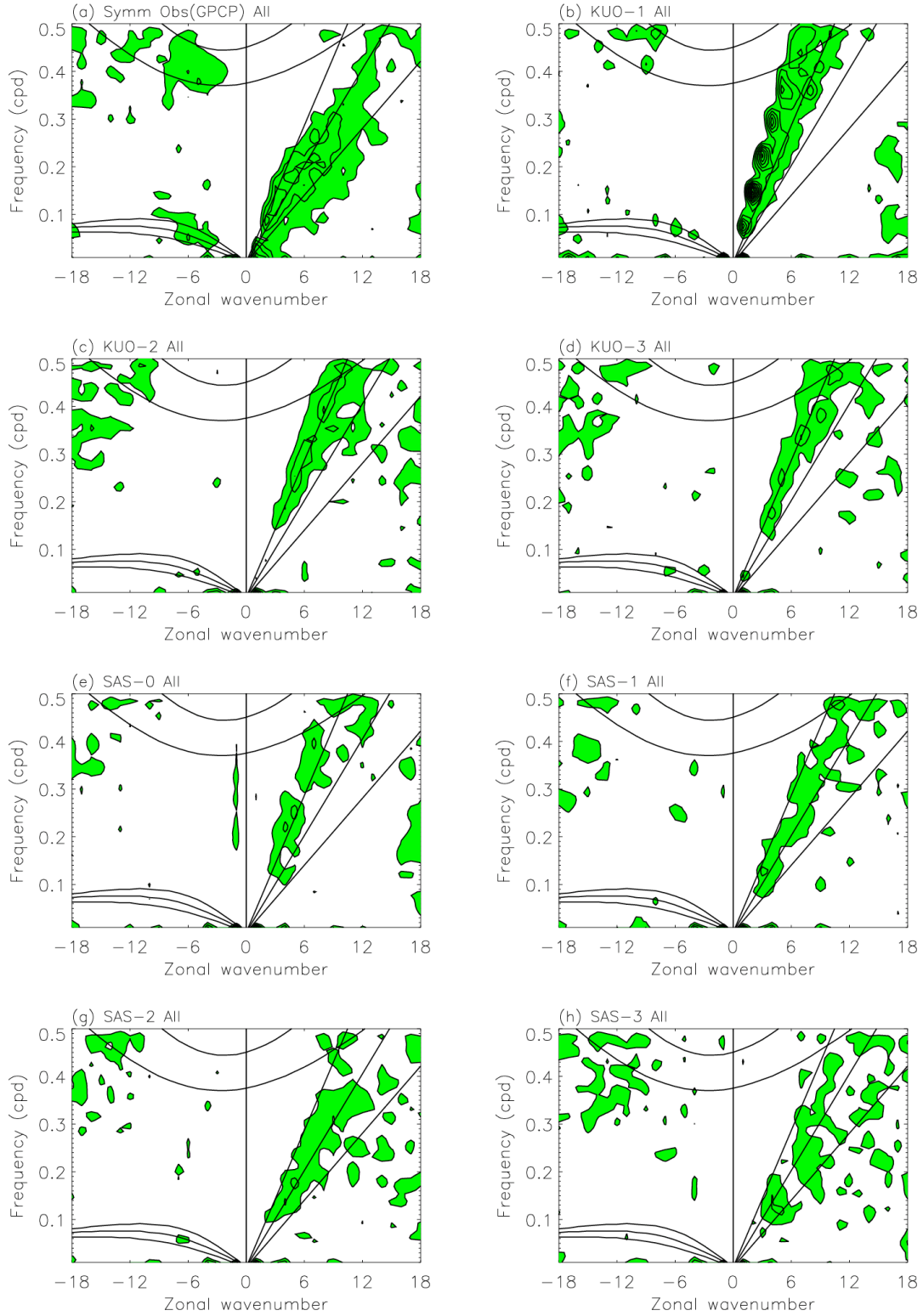


Figure 4. Space-time spectrum of 15N-15S symmetric component of precipitation divided by the background spectrum. Superimposed are the dispersion curves of the odd meridional mode-numbered equatorial waves for the five equivalent depths of 12, 25, and 50m. Frequency spectral width is 1/128 cpd.

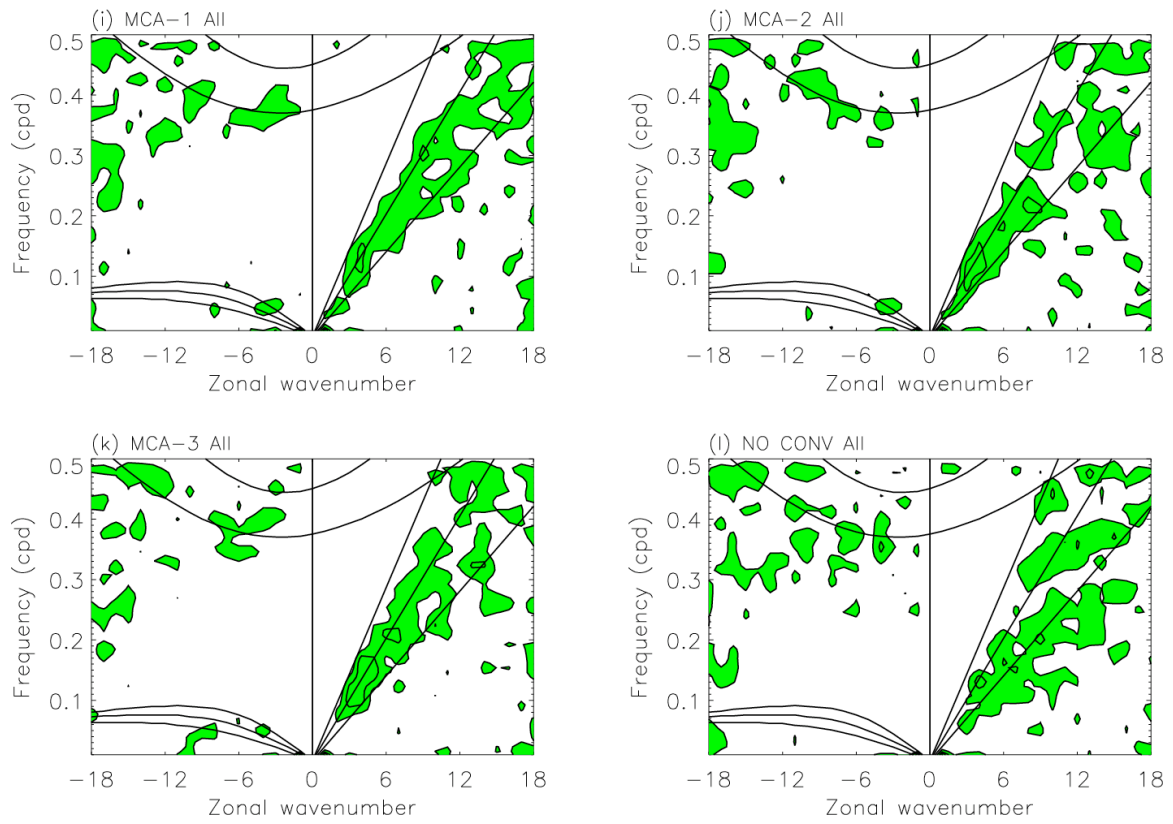


Figure 4. Continued.

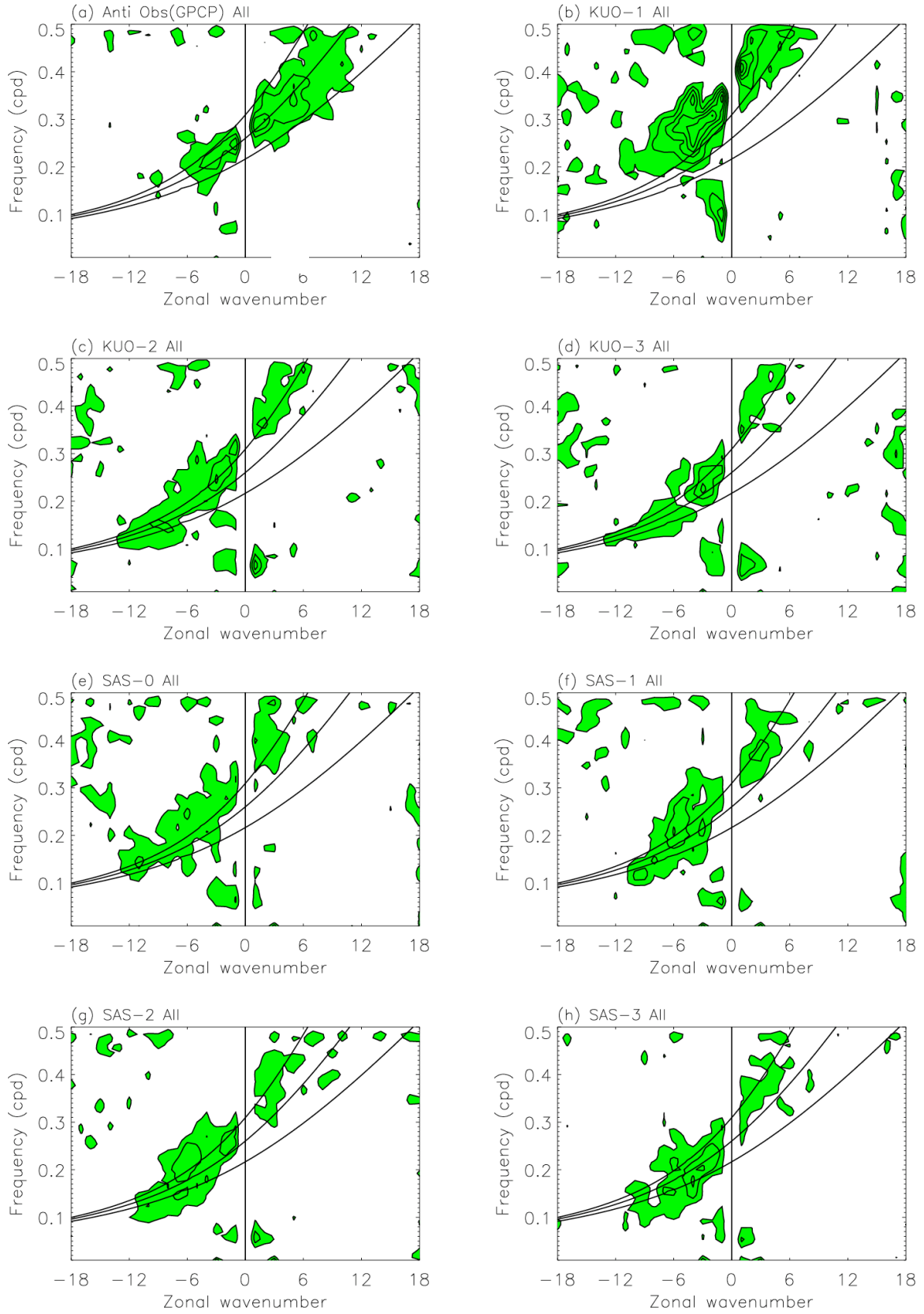


Figure 5. As in Figure 4 except for 15N-15S antisymmetric component of precipitation.

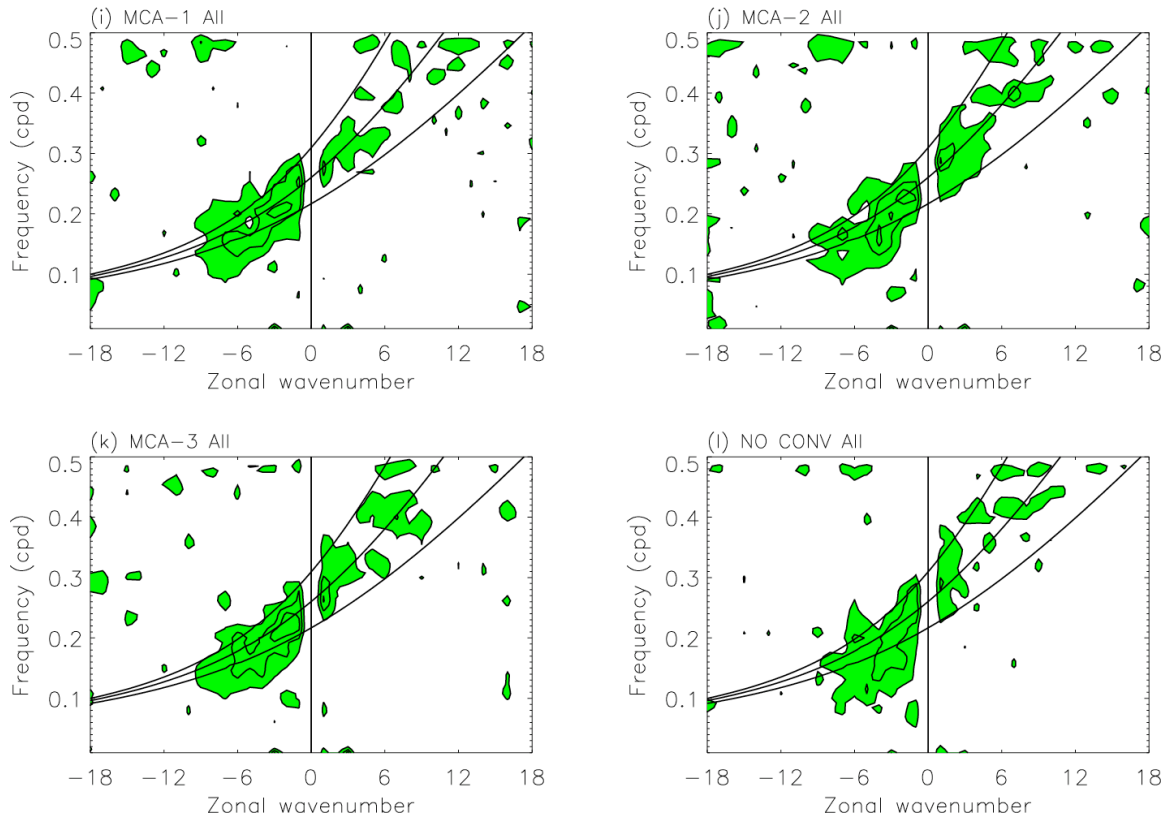


Figure 5. Continued.

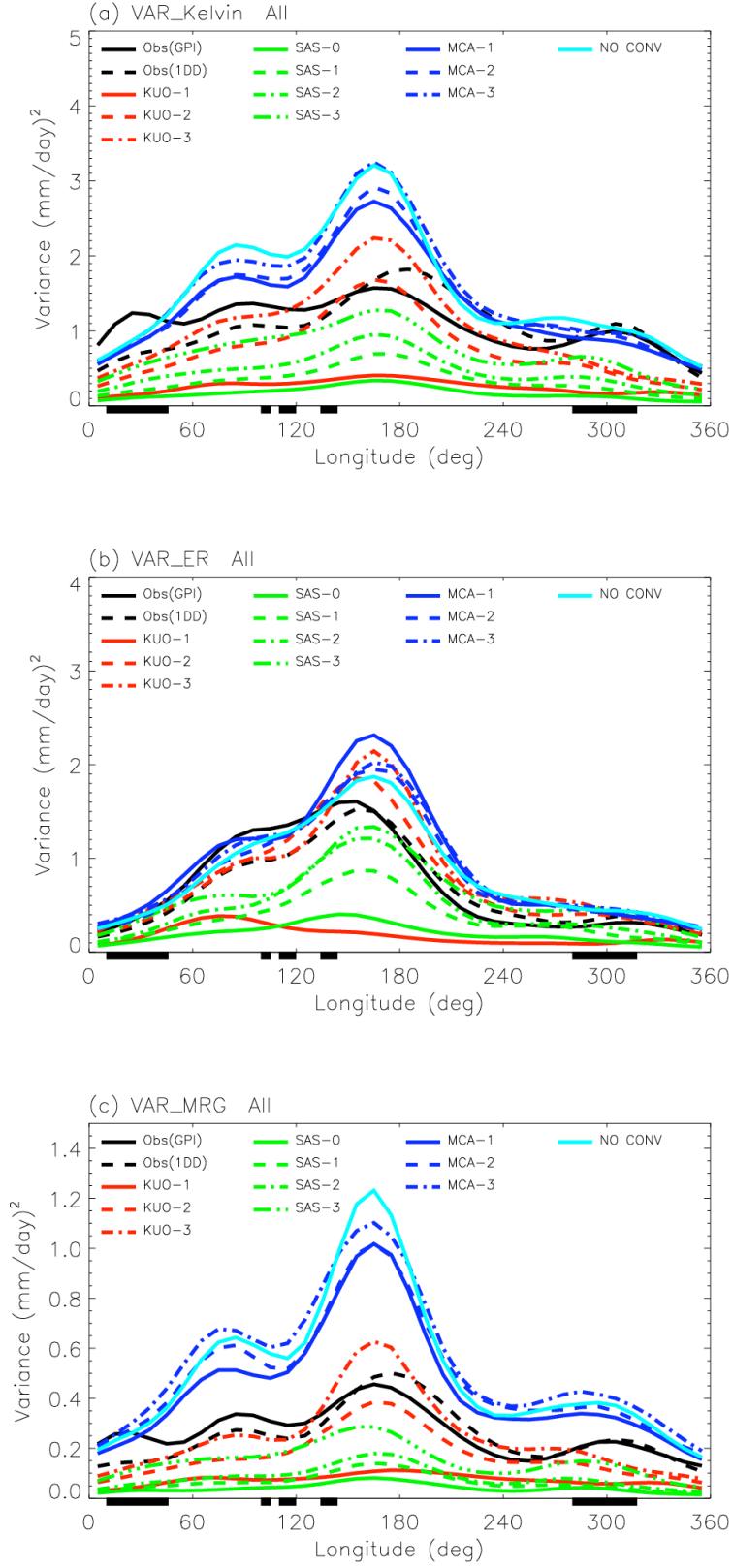


Figure 6. Variances of (a) Kelvin, (b) ER, (c) MRG, (d) EIG, and (e) WIG modes along the equator averaged between 15N and 15S.

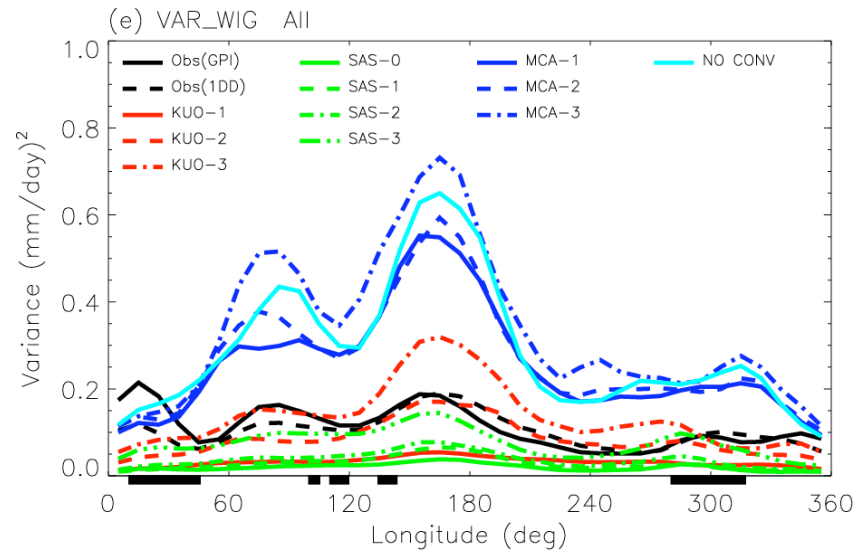
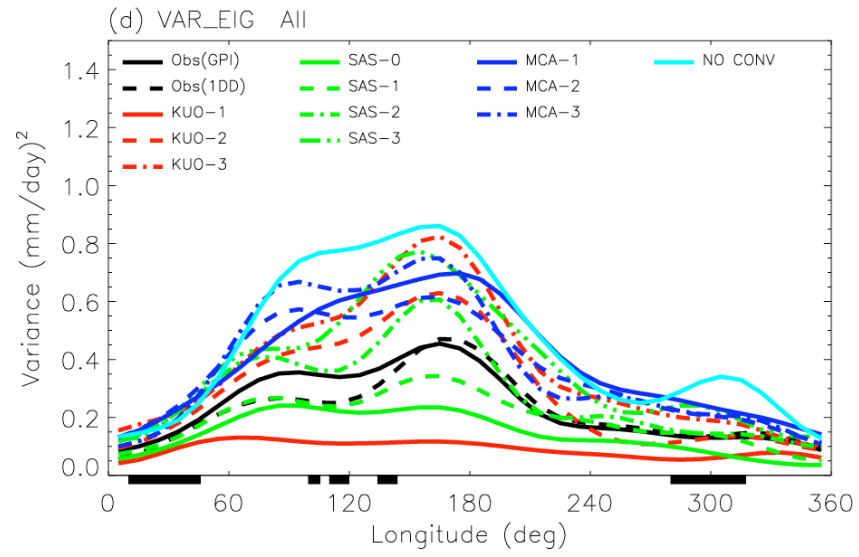


Figure 6. Continued.

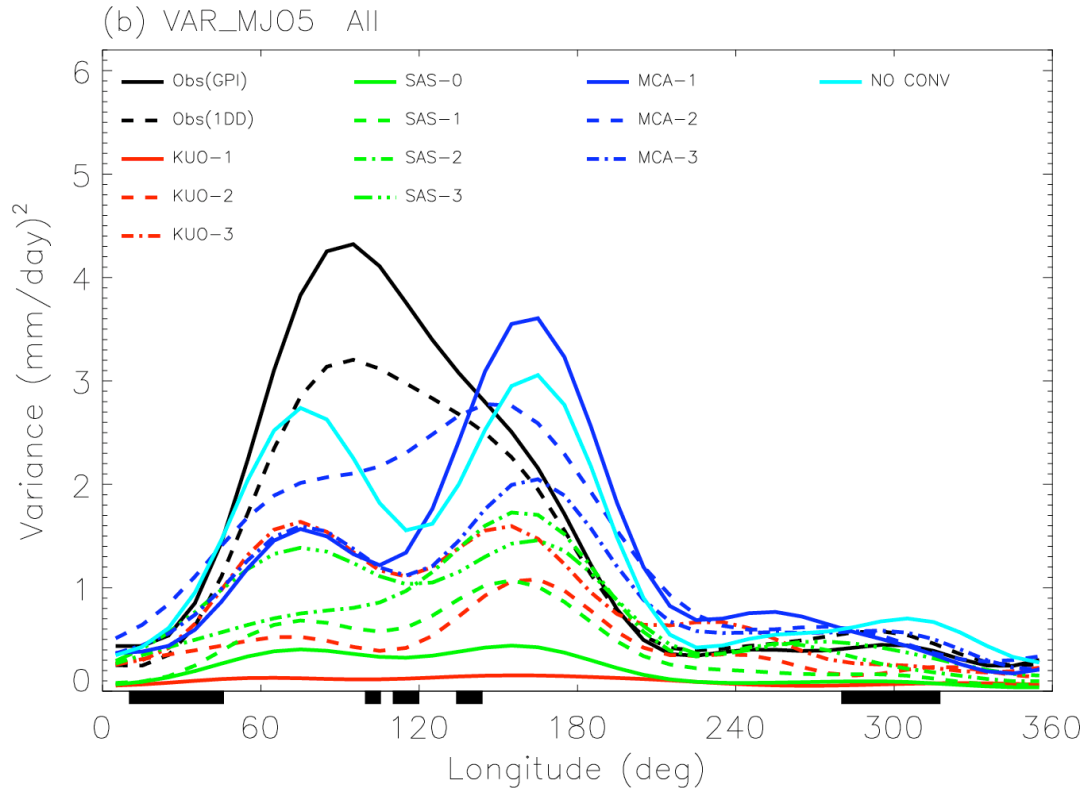
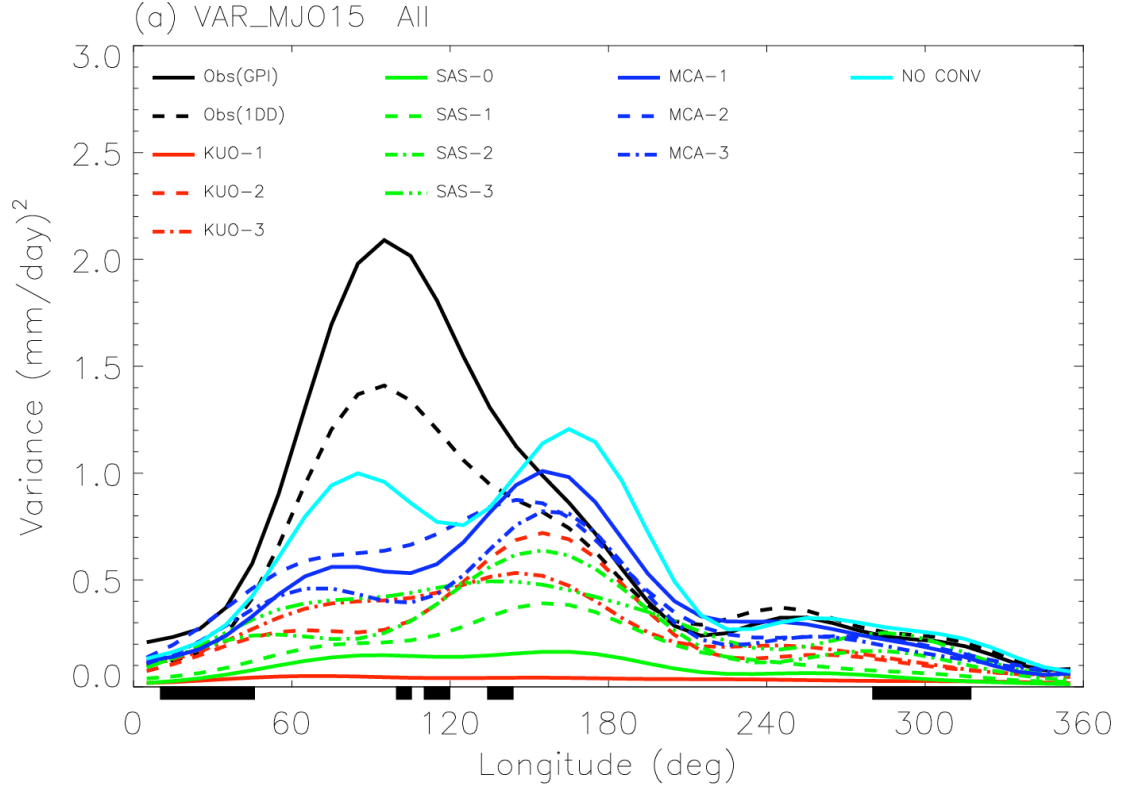


Figure 7. Variance of the MJO mode along the equator averaged between (a) 15N and 15S, and (b) 5N and 5S.

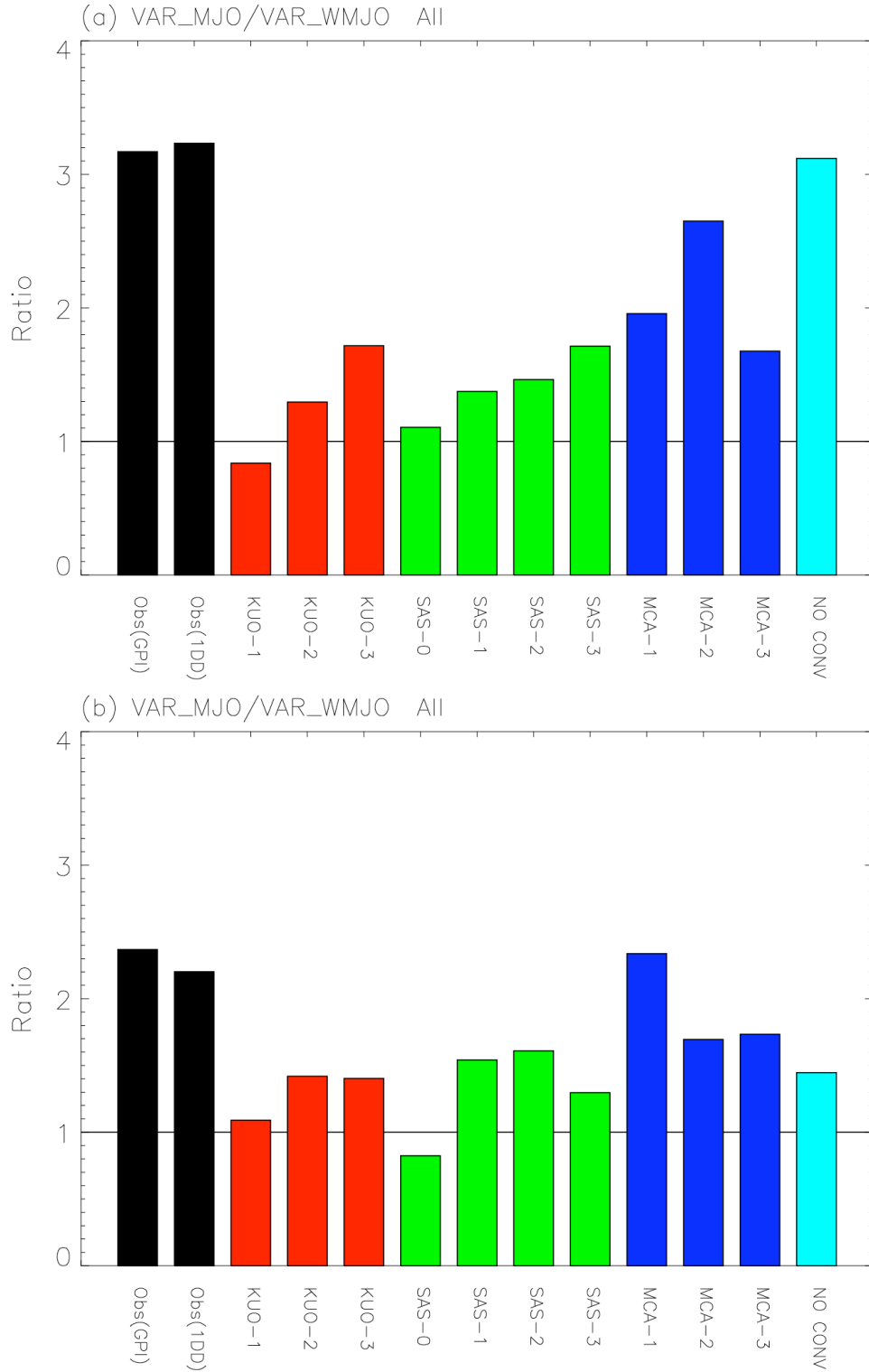


Figure 8. Ratio between the MJO variance and the variance of its westward counterpart (westward wavenumber 1-6, 30-70 day mode). The variances are averaged over (a) an Indian Ocean box between 5N-5S and 70E-100E, and (b) a western Pacific box between 5N-5S and 140E-170E.

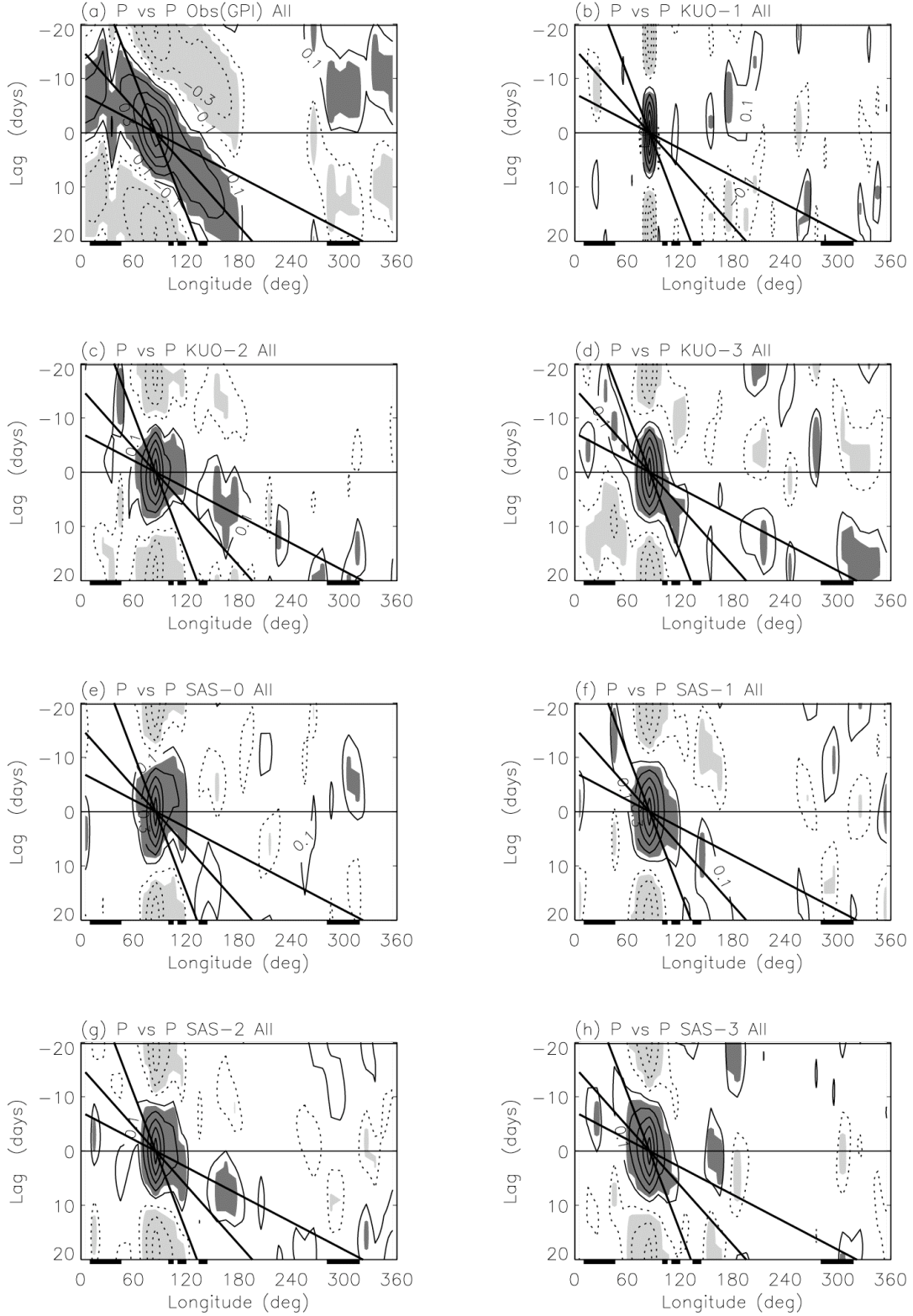


Figure 9. Lag-correlation of the 30-70 day precipitation anomaly averaged along the equator between 5N and 5S with respect to itself at 0N85E. The three thick lines correspond to phase speed of 3, 7, and 15 m/s, respectively.

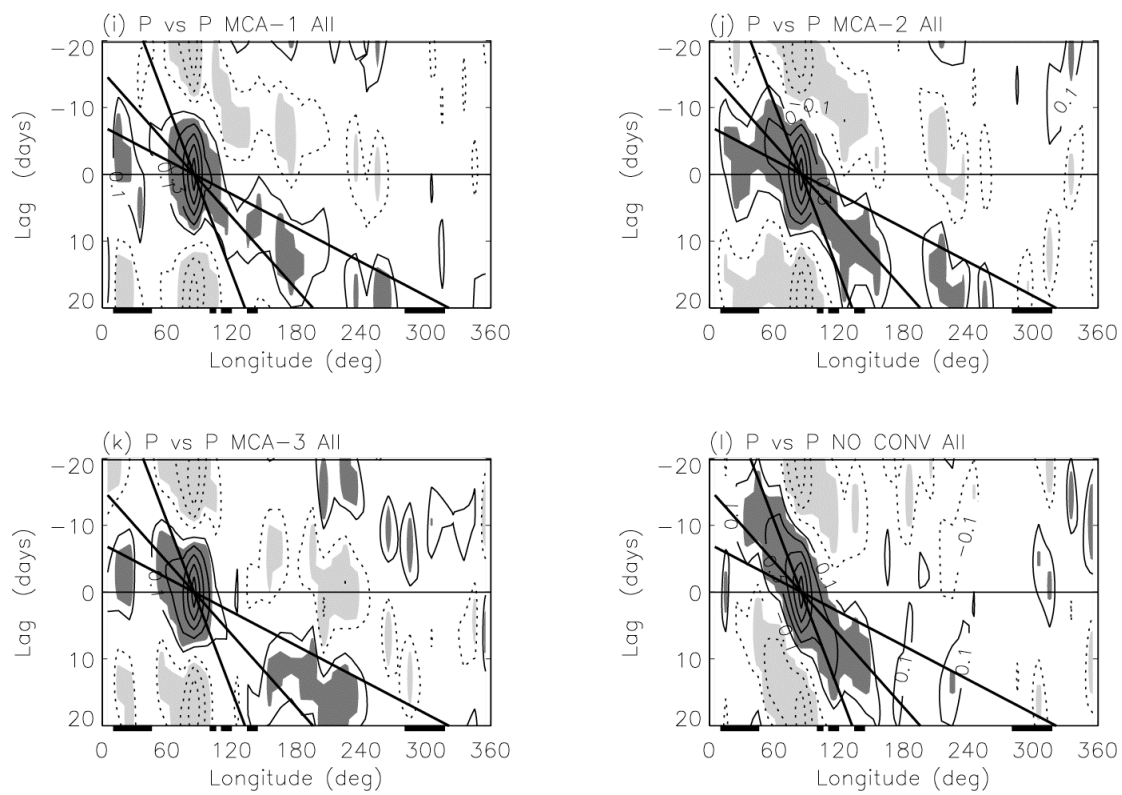


Figure 9. Continued.

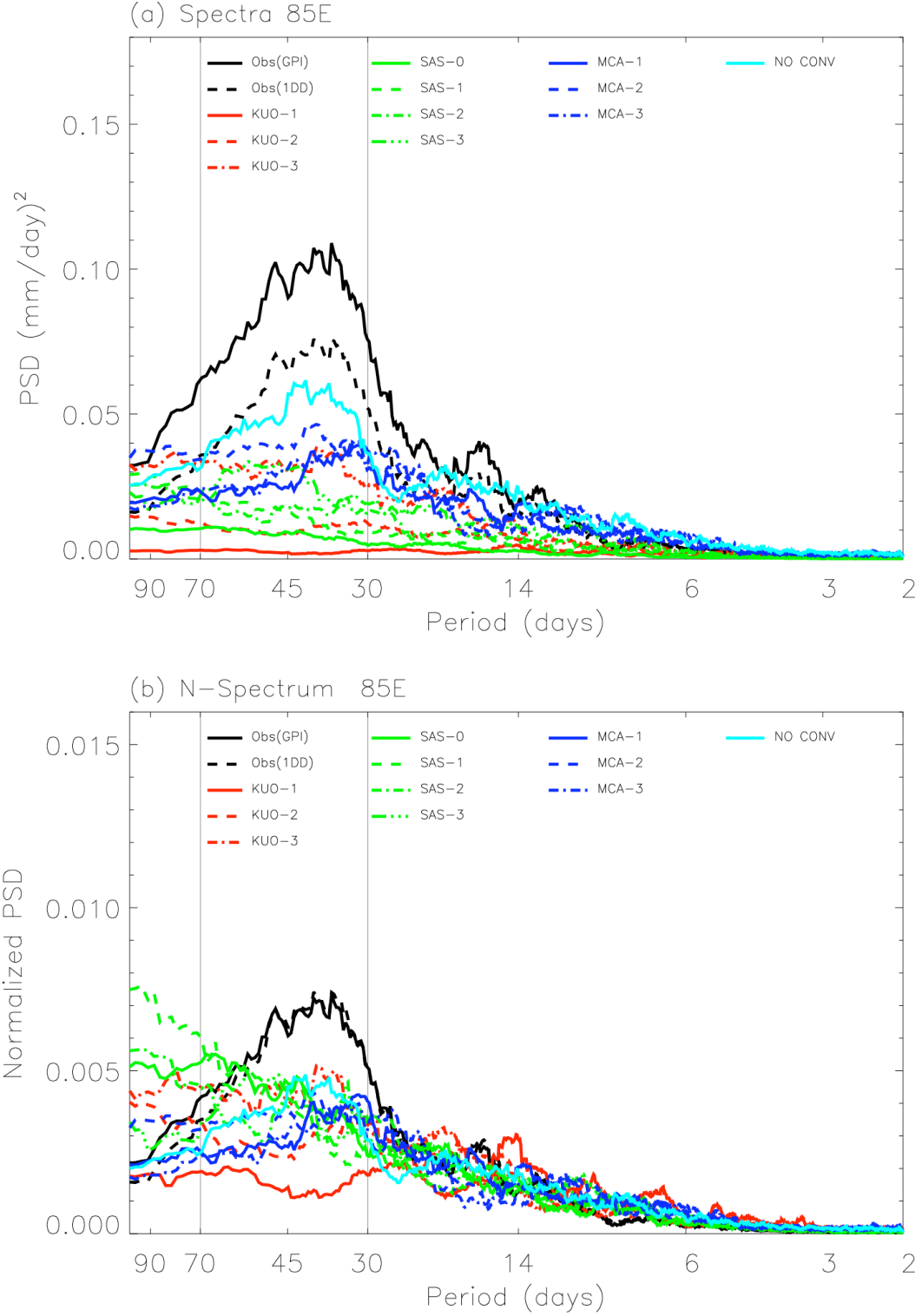


Figure 10. Spectrum of the eastward wavenumber 1-6 component of equatorial precipitation (5N-5S) at 0N155E for two observational datasets and 14 models. (a) raw spectrum; (b) normalized spectrum. Frequency spectral width 1/100 cpd.

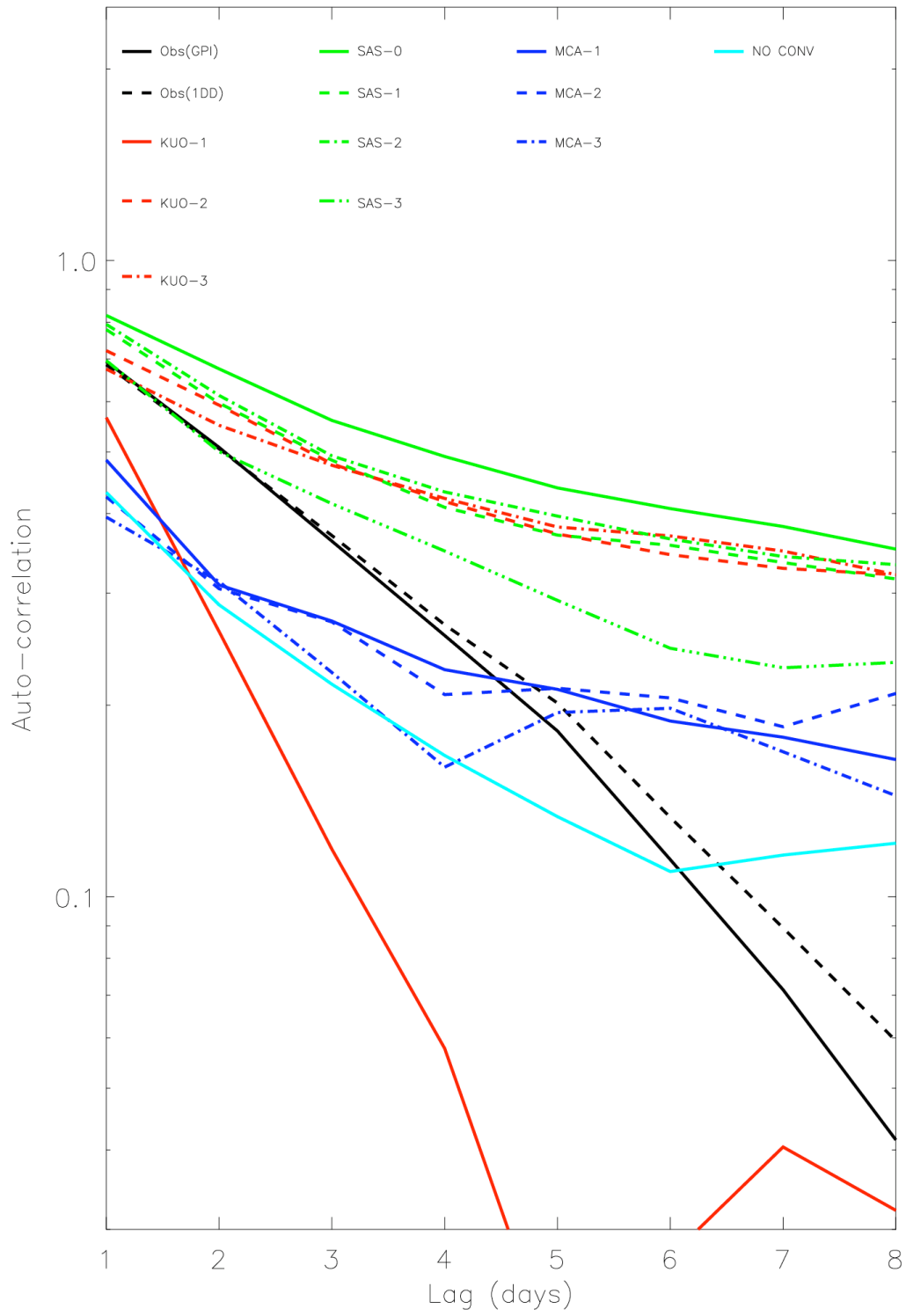


Figure 11. Auto-correlation of precipitation at 0N155E.

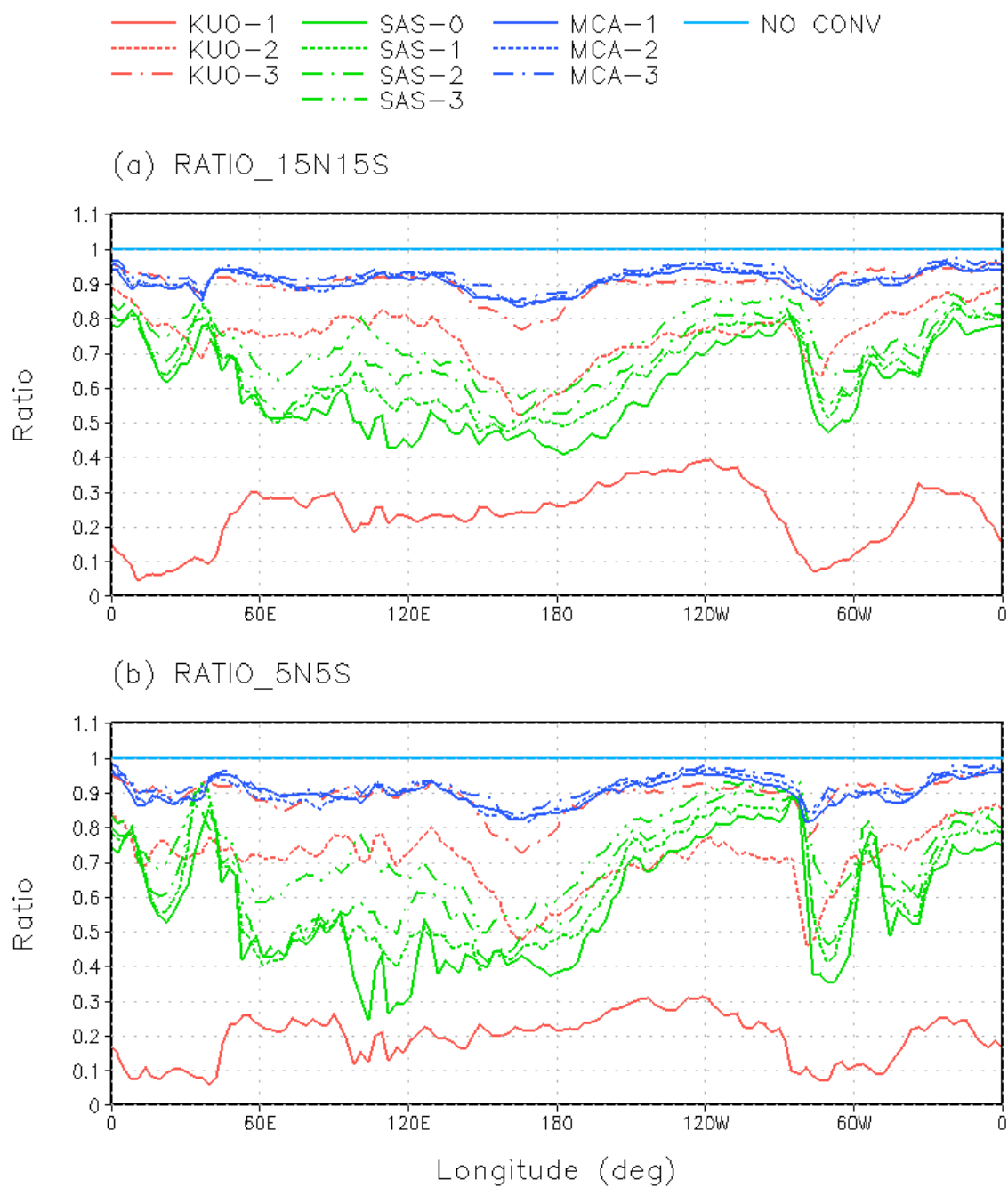


Figure 12. The ratio between time-mean large-scale precipitation and time-mean total precipitation averaged between (a) 15N-15S, and (b) 5N-5S.

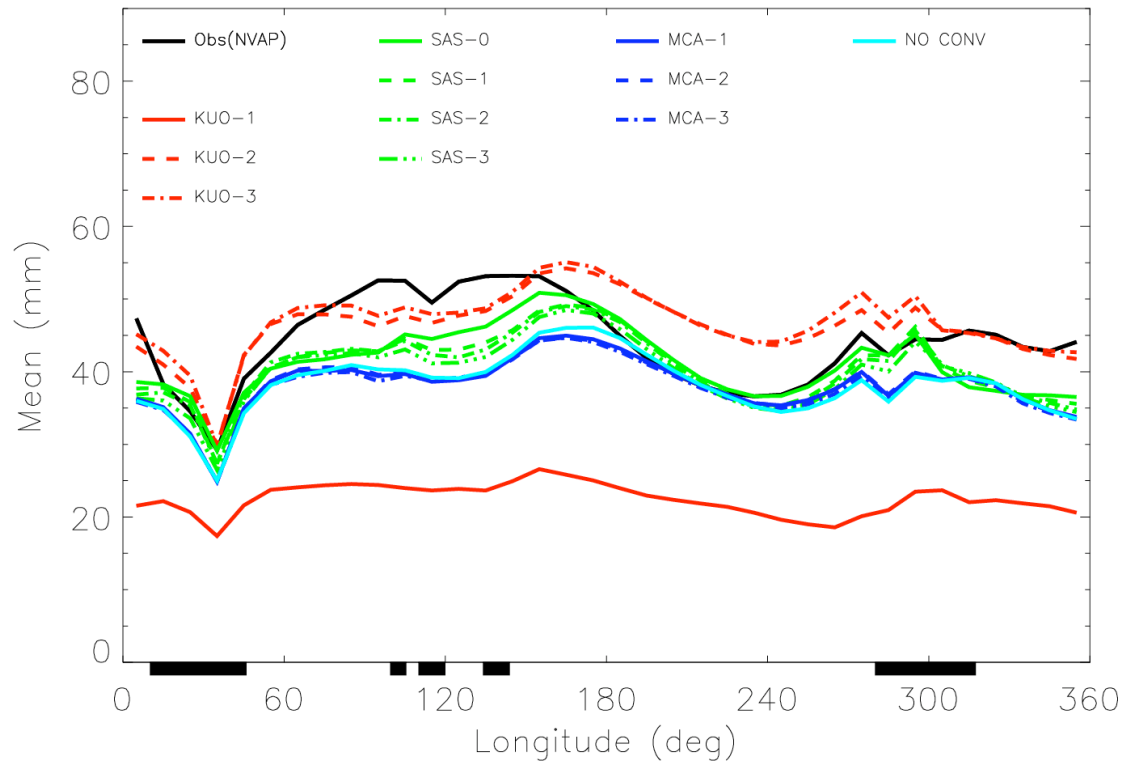


Figure 13. Annual mean total precipitable water along the equator averaged between 5N and 5S.